Computer Methods in Applied Mechanics and Engineering 457 (2026) 118929

Contents lists available at ScienceDirect

Comput. Methods Appl. Mech. Engrg.

journal homepage: www.elsevier.com/locate/cma

A unified fluid-solid elasto-viscoplastic finite element model for the simulation of 3D concrete printing across process scales

Giacomo Rizzieri [a,*], Derk Bos [b], Rob Wolfs [b], Liberato Ferrara [a], Massimiliano Cremonesi [a]

[a] Department of Civil and Environmental Engineering, Politecnico di Milano, Piazza Leonardo da Vinci 32, 20133, Milano, Italy
[b] Department of the Built Environment, Eindhoven University of Technology, P.O. Box 513, 5600 MB, Eindhoven, The Netherlands

ARTICLE INFO

Keywords:
3D Concrete Printing (3DCP)
Extrusion and layer deposition
Buildability
Particle Finite Element Method (PFEM)
Fluid-solid phase transition
Saramito constitutive law

ABSTRACT

An advanced computational approach is presented for the high-fidelity simulation of 3D Concrete Printing (3DCP) across process- and length-scales, encompassing extrusion, layer deposition, and buildability. The framework couples a flexible finite element environment with a novel constitutive model, extending Saramito elasto-viscoplastic formulation to cementitious materials for the first time. Using a limited set of experimentally identifiable parameters, the model reproduces elastic behaviour in the solid regime and provides a smooth, thermodynamically consistent transition between fluid- and solid-like states. To account for the pressure-dependent response of early-age concrete, a Drucker-Prager yield criterion is adopted, while thixotropy and structural build-up are modelled through time-dependent material properties. Large deformations and free-surface evolution, critical in the fluid regime, are resolved using the Particle Finite Element Method (PFEM), which combines an updated Lagrangian formulation with Delaunay remeshing. Additional numerical strategies are introduced to handle the complex boundary conditions associated with extrusion and layer deposition. The model is validated against 3D printing experiments involving single- and multi-layer walls, both vertical and inclined. The simulated geometries show excellent agreement with laser-scanned data and provide insight into the role of elasticity during layer deposition. Out-of-plane collapse mechanisms observed experimentally were also reproduced numerically with good reliability. Finally, full-scale simulation of a printed structural component is conducted, demonstrating the model capacity of capturing extrusion dynamics, interlayer merging, junction formation, and the overall mechanical response of the built object.

1. Introduction

3D Concrete Printing (3DCP) is reshaping the construction industry. By leveraging digital and automated workflows, it promises higher geometrical accuracy, shorter construction times, reduced material waste, and improved sustainability [1].

In practice, however, the full potential of 3DCP, including its capacity to produce optimized structural forms that would otherwise be impossible to fabricate with conventional methods, is still far from being fully achieved. Limitations in material understanding and process control [2], combined with the lack of a standardized regulatory framework, hinder its widespread adoption. These challenges stem from the intrinsic complexity of the printing process, which spans multiple spatial and temporal scales, as well as

* Corresponding author.
E-mail address: giacomo.rizzieri@polimi.it (G. Rizzieri).

https://doi.org/10.1016/j.cma.2026.118929
Received 17 December 2025; Received in revised form 20 February 2026; Accepted 15 March 2026
Available online 10 April 2026

from the highly engineered cementitious materials used. Their behaviour is tightly coupled to process parameters and sensitive to environmental conditions, often forcing practitioners to rely on trial-and-error strategies.

At the same time, the inherently digital nature of 3DCP makes it particularly well suited for integration with predictive and control-oriented methodologies. The ability to anticipate the outcome of a printing operation in fact opens the door for process optimization and real-time decision support. In this respect, while analytical formulations are often too simplified to capture the multiphysics complexity of the process [3], advanced numerical methods and, more recently, data-driven approaches have emerged as powerful tools for delivering predictive insight and supporting process design in 3DCP.

The most established numerical approaches rely on solid finite element models combined with selective layer (or element) activation to predict failure modes, such as buckling or plastic collapse, and thereby assess buildability [4,5]. Their applicability has been demonstrated for vertically non-uniform and non-planar geometries [6,7], extended to full-scale prints [8], and further enhanced through integration with advanced constitutive models that capture aging and damage [9] as well as thermal effects [10]. However, these models do not realistically capture the extrusion dynamics and typically neglect both the local plastic deformations that occur around the nozzle and the non-negligible pressure increments that develop beneath it. Moreover, the deposited filament is still often idealized as a simple geometric shape – most commonly a rectangle – thereby overlooking the actual cross-sectional profile formed during deposition. This geometric simplification may affect structural failure predictions and lead to an overestimation of buildability [11,12].

Fluid-based computational approaches, in contrast, enable geometrically faithful simulations of key stages of the 3D printing process, including pumping, extrusion, and layer deposition. In particular, continuum fluid models developed using the Finite Volume Method (FVM) [13–15] and the Particle Finite Element Method (PFEM) [16,17] have demonstrated high accuracy in predicting filament shapes for single or a few superimposed layers. These models can also be used to assess filament morphology and identify potential defects such as filament tearing, slugs, or filament buckling [15,18].

Most of the fluid-based approaches rely on viscoplastic rheological laws (e.g., Bingham or Herschel-Bulkley), which are effective at capturing the flow behaviour and stoppage of fresh concrete, but provide an unrealistic description of the material's response in the solid state. Various remedies have been proposed to enhance constitutive modelling, ranging from incorporating thixotropy in the Bingham law [19] to the use of Bingham's model extension available in FLOW3D [13,15]. However, efficiently introducing elasticity into a fluid-based framework – while preserving a smooth, thermodynamically consistent fluid-solid transition – is not trivial and has long remained an open problem.

Moreover, existing fluid approaches remain unable to simulate the entire printing process within a single, continuous framework. This is partly because many solvers are inherently tailored to CFD rather than solid mechanics, and partly because even more flexible methods (e.g., PFEM) have so far been applied mainly to extrusion simulations [17] or require combination with layer-activation strategies to handle larger prints [12]. Additionally, achieving high geometric fidelity in full-scale simulations comes with prohibitive computational costs [20].

Similar to continuum fluid approaches, meshfree methods, including the Discrete Element Method (DEM), Smoothed Particle Hydrodynamics (SPH), or discrete lattice modelling, have been applied to realistically simulate extrusion and gain insight into the mixing and pumping phases [21,22], or buildability [23,24]. However, the development of physically meaningful constitutive laws for these methods remains a significant challenge, frequently necessitating extensive calibration, and full-scale simulations are generally also computationally prohibitive.

Overall, simulation of 3DCP remains largely divided into two main classes of methods: those focusing on the extrusion scale, which employ fluid-based techniques, and those targeting the structural scale, which adopt solid-like approaches. This division is primarily due to the absence of constitutive models that are simultaneously simple, robust, and capable of reproducing both fluid and solid states, as well as the lack of unified computational frameworks for both fluid and solid mechanics. Computational cost also plays a major role; however if advances in CPU/GPU parallelization and machine-learning-assisted simulation may help alleviate these challenges in the future, a holistic framework for unified fluid-to-solid simulation across all 3DCP process scales is still lacking.

The objective of this article is twofold. First, we introduce a novel advanced constitutive law that describes fresh cementitious materials seamlessly across fluid and solid phases. The model adopts a Saramito-type formulation that ensures a smooth, thermodynamically consistent transition from viscous or viscoelastic flow to neo-Hookean elasticity, with the option to incorporate creep in the solid regime. For the first time, this framework is tailored to cement-based materials by incorporating pressure sensitivity through a Drucker-Prager yield surface and by accounting for the time-dependent evolution of the mechanical response arising from thixotropy and structural build-up. A detailed description is provided in Section 2.

Second, the constitutive law is embedded within a Particle Finite Element Method (PFEM) framework, which combines an updated Lagrangian formulation with efficient Delaunay-based remeshing to handle large displacements, free-surface evolution, and topological changes of the domain. Unlike standard FEM solvers, which typically require separate models or complex coupling strategies to transition between fluid and solid behaviour, PFEM provides a continuous and unified treatment of the material response across phases.

Within this framework, *ad hoc* computational techniques have been developed and implemented to reproduce the 3D printing process with high fidelity across different scales, as detailed in Section 3. The model captures processes ranging from extrusion and layer deposition, governed by fluid-like behaviour, to the global solid-like mechanical response at the scale of the object, including elasto-plastic deformations and out-of-plane buckling collapse. Furthermore, the framework employs a partitioned solution strategy for the elasto-viscoplastic equations, combined with a CPU-parallelised implementation, substantially reducing computational cost and enabling full-scale simulations that would otherwise require layer-activation techniques.

Finally, the predictive capabilities of the proposed model are demonstrated in Section 4 through an extensive validation campaign conducted at TU Eindhoven. The campaign includes the printing of multi-layer vertical and inclined walls, with validation performed by comparing numerically predicted cross-sectional profiles to laser scans. This analysis revealed the influence of substrate elasticity on layer deposition and filament profiles. Subsequently, the full 3D printing process was simulated for the walls, including out-of-plane collapse, allowing assessment of the model's buildability predictions against experimental observations. A more complex structural component exhibiting in-plane layer merging was then simulated to showcase the model's ability to handle intricate geometries and provide high-fidelity estimates of joint and corner shapes.

2. Continuum model

2.1. Momentum and mass balance

For the formulation of the governing equations, fresh concrete is idealized as a homogeneous, isothermal, incompressible material. The equations are expressed within the framework of an Arbitrary Lagrangian-Eulerian (ALE) description, which allows the computational mesh to move independently of the material flow [25]. Let Ω_t denote the evolving fluid domain over the time interval $[0,T]$. The spatial position in the current configuration is represented by $\boldsymbol{x}$, whereas χ denotes the reference coordinates associated with the moving mesh. Under these assumptions, the balance of linear momentum and the mass continuity equation can be written as:

$$\rho\frac{d\boldsymbol{u}}{dt} = \nabla_{\boldsymbol{x}}\cdot\boldsymbol{\sigma} + \rho\boldsymbol{b} \quad \text{in } \Omega_t\times[0,T], \tag{1}$$

$$\nabla_{\boldsymbol{x}}\cdot\boldsymbol{u} = 0 \quad \text{in } \Omega_t\times[0,T], \tag{2}$$

where ρ is the (constant) density, $\boldsymbol{u}=\boldsymbol{u}(\boldsymbol{x},t)$ is the velocity field, $p=p(\boldsymbol{x},t)$ is the pressure field, $\boldsymbol{\sigma}=\boldsymbol{\sigma}(\boldsymbol{x},t)$ is the Cauchy stress tensor, $\boldsymbol{b}$ is the vector of the external accelerations and $\frac{d(\bullet)}{dt}=\frac{\partial(\bullet)}{\partial t}\Big|_{\chi}+\boldsymbol{c}\cdot\nabla_{\boldsymbol{x}}(\bullet)$ represents the total time derivative, with $\boldsymbol{c}$ being the convective velocity (i.e., the relative velocity between the mesh and the material points).

A suitable set of initial and boundary conditions must also be prescribed:

$$\boldsymbol{u}(\boldsymbol{x},t=0)=\boldsymbol{u}_0(\boldsymbol{x}) \quad \text{in } \Omega_0, \tag{3}$$

$$p(\boldsymbol{x},t=0)=p_0(\boldsymbol{x}) \quad \text{in } \Omega_0, \tag{4}$$

$$\boldsymbol{u}(\boldsymbol{x},t)=\widetilde{\boldsymbol{u}}(\boldsymbol{x},t) \quad \text{on } \Gamma_D\times(0,T), \tag{5}$$

$$\boldsymbol{\sigma}\cdot\boldsymbol{n}=\boldsymbol{h}(\boldsymbol{x},t) \quad \text{on } \Gamma_N\times(0,T), \tag{6}$$

where $\boldsymbol{u}_0$, p_0, $\widetilde{\boldsymbol{u}}$, $\boldsymbol{h}$, are given known functions and $\boldsymbol{n}$ is the outward normal to the boundary $\Gamma_t=\partial\Omega_t$, which is subdivided into two non-overlapping subsets, Γ_D and Γ_N, such that $\Gamma_D\cup\Gamma_N=\Gamma_t$ and $\Gamma_D\cap\Gamma_N=\emptyset$.

Finally, to complete the formulation, it is recalled that in fluid mechanics the Cauchy stress tensor is commonly decomposed into a volumetric and a deviatoric part:

$$\boldsymbol{\sigma} = -p\boldsymbol{I} + \boldsymbol{\tau}(\dot{\boldsymbol{\epsilon}},\boldsymbol{\epsilon}), \tag{7}$$

where $\boldsymbol{I}$ denotes the identity tensor and $\boldsymbol{\tau}$ the deviatoric stress tensor, which must be evaluated through a suitable constitutive law relating it to the deviatoric strain $\boldsymbol{\epsilon}$ or strain-rate $\dot{\boldsymbol{\epsilon}}$ tensors. Particularly, the deviatoric strain rate tensor is defined as:

$$\dot{\boldsymbol{\epsilon}}(\boldsymbol{u}) = \frac{1}{2}(\nabla_{\boldsymbol{x}}\boldsymbol{u}+\nabla_{\boldsymbol{x}}\boldsymbol{u}^T) - \frac{1}{3}(\nabla_{\boldsymbol{x}}\cdot\boldsymbol{u})\boldsymbol{I}. \tag{8}$$

This definition implies that, for an incompressible fluid, the deviatoric strain-rate (or strain) tensor coincides with the total strain-rate (or strain) tensor.

2.2. Constitutive law

We propose a novel, simple yet flexible constitutive model for 3D-printable cement-based materials. The formulation is inspired by the elasto-viscoplastic Saramito model [28,29], originally developed to describe the behaviour of complex fluids with embedded microstructures (e.g., foams, emulsions and gels). We show that Saramito's model provides an excellent foundation for representing the rheological response of fresh and early-age cementitious materials, which can be viewed as particle-laden suspensions composed of a water-based fluid matrix and interacting solid particles [26,27].

At the continuum level the proposed model, conceived as an extension of Saramito's formulation, is developed within the same rigorous theoretical framework and inherits many of its desirable properties:

- The model is consistently derived within the framework of *generalized standard materials* by differentiation of strictly convex free energy and dissipation potentials, thereby guaranteeing compliance with the second law of thermodynamics [28,29].
- The model provides a smooth and physically consistent transition between the solid-like and fluid-like regimes [28–30].
- The elastic contribution ensures that the stress tensor remains well-defined and physically meaningful even below the yield limit, in the solid state. This feature makes the model in better agreement with experimental observations and also removes the need for regularization techniques often required in purely viscoplastic formulations [31].

2.2.1. Proposed model

To capture the specific physics and behaviour of cementitious materials, the original Saramito's model is extended as follows:

1. **Time-dependent structuration**: Fresh concrete, once deposited, undergoes both reversible and irreversible structuration processes due to thixotropy and early-age hydration. To capture these effects, both the elastic modulus and the yield surface are assumed to evolve with time. Generally, a linear increment with time according to Roussel's model [32] or an exponential one [33] are adopted.
2. **Pressure-sensitive yielding**: Owing to its partially granular nature, early age concrete exhibits a pressure-dependent mechanical response. Accordingly, the von Mises yield criterion used in the original Saramito model is here replaced by the more general Drucker-Prager (DP) frictional criterion. The DP surface can expand with increasing hydrostatic pressure, while remaining smoother and more numerically tractable than the Mohr-Coulomb counterpart.

A schematic representation of the proposed model, hereafter referred to as the "*Saramito-DP*" model, is shown in Fig. 1.

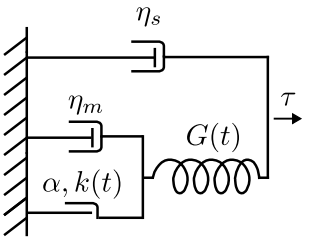

Fig. 1. 1D *Saramito-DP* model, consisting of a spring of stiffness $G(t)$, two dashpots one associated to the solvent viscosity η_s and the other to the microstructure viscosity η_m, and a pressure-sensitive dry-friction element with stress threshold depending on Drucker-Prager yield criterion parameters $\alpha, k(t)$.

The proposed constitutive framework, consistent with the standard Saramito model, reproduces a material that behaves as an incompressible neo-Hookean viscoelastic solid in the pre-yield regime and as an Oldroyd-B viscoelastic fluid beyond yielding. Referring to the one-dimensional rheological scheme in Fig. 1, the components of the elasto-viscoplastic model can be clearly identified. The upper branch represents the fluid matrix, or "solvent", modeled as a Newtonian dashpot with viscosity η_s. The lower branch accounts for the microstructural, or "solute", contribution and consists of a Maxwell element composed of a spring with time-dependent stiffness $G(t)$, a dry-friction element governed by Drucker-Prager plasticity ($k(t)$, α), and a viscous damper with viscosity η_m representing the microstructural viscosity. In this formulation, the spring stores elastic potential energy, whereas viscous and frictional plasticity mechanisms dissipate it.

Following the physics of ideal elasto-viscoplastic fluids, where a Newtonian solvent and an internal solute microstructure can generally be clearly identified, in this work, *Saramito-DP*'s model is written separating the solvent ($\boldsymbol{\tau}_s$) and micro-structure ($\boldsymbol{\tau}_m$) contributions in the deviatoric part of the Cauchy stress tensor:

$$\boldsymbol{\tau} = \boldsymbol{\tau}_s + \boldsymbol{\tau}_m. \tag{9}$$

The solvent contribution consists of a standard Newtonian viscous term, while the micro-structure contribution is defined implicitly through the following evolution equation:

$$\boldsymbol{\tau}_s = 2\eta_s \dot{\boldsymbol{\epsilon}}, \tag{10}$$

$$\lambda(t)\overset{\triangledown}{\boldsymbol{\tau}}_m + \beta_{fs}(t)\boldsymbol{\tau}_m = 2\eta_m \dot{\boldsymbol{\epsilon}}, \tag{11}$$

where $\boldsymbol{\tau}_m$ denotes the deviatoric stress associated with the internal microstructure, $\overset{\triangledown}{(\bullet)}$ denotes the upper-convected time derivative [34], defined for any second-order tensor $\boldsymbol{A}$ as:

$$\overset{\triangledown}{\boldsymbol{A}} = \frac{\partial \boldsymbol{A}}{\partial t} + \boldsymbol{u}\cdot\nabla\boldsymbol{A} - \boldsymbol{A}\cdot\nabla\boldsymbol{u} - (\nabla\boldsymbol{u})^T\cdot\boldsymbol{A}, \tag{12}$$

$\lambda(t) = \frac{\eta_m}{G(t)}$ denotes the microstructure relaxation time, with $G(t)$ being the elastic shear modulus characterizing the material's time-dependent stiffness, and $\beta_{fs}(t)$ is the coefficient controlling the fluid-to-solid phase transition. In the present formulation, $\beta_{fs}(t)$ governs mechanically-induced phase transitions and is therefore defined as a stress-dependent quantity. It also depends on yield-related material properties, which evolve with time. This time dependence allows $\beta_{fs}(t)$ to indirectly capture the influence of both physical processes, such as thixotropy, and chemical processes, such as cement hydration, on the mechanical response. Specifically, $\beta_{fs}(t) \in [0, 1]$ is defined as:

$$\beta_{fs}(t) = \max\left(0, \frac{\|\boldsymbol{\tau}_m\| - \tau_{0,DP}(t)}{\|\boldsymbol{\tau}_m\|}\right), \tag{13}$$

where $\|\bullet\|$ is the von Mises norm and $\tau_{0,DP}$ a time dependent pressure-sensitive yield stress value.

According to the Drucker-Prager yield criterion, the yield stress $\tau_{0,DP}(t)$ can be expressed as:

$$\tau_{0,\mathrm{DP}}(t) = k(t) + \alpha\overline{p}(t), \tag{14}$$

where $\overline{p}(t) = \max(0,\, p(t))$ is the pressure (positive in compression), with a cut-off introduced to prevent tensile pressures from contracting the yield surface, consistent with the behaviour of fresh concrete, $k(t)$ is a time-dependent cohesion-related parameter, and α a friction coefficient. This formulation derives directly from the standard Drucker-Prager yield function, formulated in terms of the first invariant of the stress tensor $I_1 = \mathrm{tr}(\boldsymbol{\sigma}) = 3p$, and the second invariant of the deviatoric stress tensor $J_2 = \frac{1}{2}\boldsymbol{\tau} : \boldsymbol{\tau}$, as

$$F(\boldsymbol{\sigma}, t) = \sqrt{J_2} + \frac{\alpha}{3} I_1 - k(t) = 0. \tag{15}$$

The Drucker-Prager model can be regarded as an extension of the von Mises yield criterion that incorporates pressure sensitivity, or equivalently, as a smooth approximation of the Mohr-Coulomb failure envelope [35]. This latter interpretation is particularly convenient, as it allows the parameters α and $k(t)$ to be determined by fitting the Drucker-Prager cone to the Mohr-Coulomb hexagonal yield surface. Particularly, for a circumscribed Drucker-Prager surface, the parameters are given by

$$k(t) = \frac{6c(t)\cos\phi}{\sqrt{3}(3 - \sin\phi)}, \tag{16}$$

$$\alpha = \frac{6\sin\phi}{\sqrt{3}(3 - \sin\phi)}, \tag{17}$$

where $c(t)$ denotes the cohesion and ϕ the friction angle of the material, as defined under the assumption of a Mohr-Coulomb failure criterion.

2.2.2. Saramito's model as a sub-case

It is instructive to note that, when the frictional behaviour is neglected, the Drucker-Prager formulation naturally reduces to von Mises plasticity [35]. Specifically, by setting $\phi = 0$ in eqs. (16) and (17), the Drucker-Prager parameters become $\alpha = 0$ and $k(t) = 2c(t)/\sqrt{3} = \tau_{0,\mathrm{VM}}(t)$, where $\tau_{0,\mathrm{VM}}(t)$ denotes the equivalent time-dependent von Mises yield stress. Consequently, the yield function particularizes to:

$$F(\boldsymbol{\tau}, t) = \sqrt{J_2} - \tau_{0,\mathrm{VM}}(t) = 0. \tag{18}$$

We can therefore conclude that the proposed *Saramito-DP* model also encompasses the time-dependent version of the standard Saramito model as a specific subcase, depending on whether the coefficient $\beta_{fs}(t)$ is expressed in terms of $\tau_{0,\mathrm{VM}}(t)$ or $\tau_{0,\mathrm{DP}}(t)$.

2.2.3. Bingham's model as a sub-case

Furthermore, by neglecting frictional effects and elasticity - i.e., for a vanishing friction angle ($\phi = 0$) and in the limit of an infinite shear modulus ($G \to \infty$) - the *Saramito-DP* model reduces to the classical Bingham model, with an equivalent plastic viscosity $\eta = \eta_s + \eta_m$ [36]. Owing to its simplicity, the Bingham model has been widely adopted to describe viscoplastic materials, which behave as rigid solids when the von Mises norm of the applied stress is below the yield stress and flow as Newtonian fluids once the yield stress is exceeded. Mathematically, the Bingham's model reads:

$$\boldsymbol{\tau}(\boldsymbol{u}, t) = 2\eta\dot{\boldsymbol{\epsilon}}(\boldsymbol{u}) + \tau_{0,VM}(t)\frac{\dot{\boldsymbol{\epsilon}}(\boldsymbol{u})}{\|\dot{\boldsymbol{\epsilon}}(\boldsymbol{u})\|} \qquad \text{if } \|\boldsymbol{\tau}\| > \tau_{0,VM}(t), \tag{19}$$

$$\dot{\boldsymbol{\epsilon}}(\boldsymbol{u}) = \mathbf{0} \qquad \text{otherwise}, \tag{20}$$

Numerically, for sufficiently large values of the shear modulus, Saramito's model already reproduces the behaviour of a purely viscoplastic material described by the Bingham model. However, solving the governing equations in the exact limit $G \to \infty$ requires a suitable regularization. Since the Bingham model is employed in the following for comparison purposes, the Papanastasiou exponential regularization [37] is adopted, which is expressed as:

$$\boldsymbol{\tau}(\boldsymbol{u}, t) = \left[2\eta + \frac{\tau_{0,VM}(t)}{\|\dot{\boldsymbol{\epsilon}}(\boldsymbol{u})\|}(1 - e^{-m\|\dot{\boldsymbol{\epsilon}}(\boldsymbol{u})\|})\right]\dot{\boldsymbol{\epsilon}}(\boldsymbol{u}), \tag{21}$$

where m is a regularization parameter governing the quality of the approximation and in this work it is set to $m = 2000\ s$.

2.3. Identification of the model's parameters

All parameters of the model possess a clear physical meaning and can be experimentally identified through appropriate mechanical or rheological tests. Depending on the desired level of detail and complexity, either the full *Saramito-DP* model or one of its simplified sub-cases can be employed. This choice can be guided by the amount and quality of experimental data available for parameter identification.

2.3.1. Yield stress and elastic shear modulus

In this work, Uniaxial Unconfined Compression Tests (UUCTs) were performed on the material at different curing ages to obtain the compressive stress–strain curves and their time evolution, following the procedure illustrated in [4]. From the curves the Young's modulus $E(t)$, Poisson's ratio ν, and compressive strength $\sigma_c(t)$ were extracted and converted into shear modulus $G(t)$ and yield strength $\tau_0(t)$ values at different ages. Alternative experimental methods [38] can also be used to determine all or some of these parameters and their time-evolution, including direct shear tests, ultrasonic tests, slug tests and flow table tests.

2.3.2. Cohesion and friction angle

For pressure-sensitive materials, an additional parameter - the internal friction angle, ϕ - must be determined. In this study, ϕ was estimated from the indentation tests reported in [39], which also show how this parameter remains relatively constant in time. By combining the friction angle with the compressive strength, the material's cohesion can be calculated. Subsequently, the Drucker-Prager parameters, α and $k(t)$, are computed from the friction angle and cohesion with equations (16,17).

2.3.3. Viscosities in the fluid regime

The total viscosity η can be measured, for example, through a flow-curve test performed on a rotational rheometer. A practical approximation of its decomposition into solvent and microstructural contributions [26] can be obtained by assuming that the solvent viscosity lies between that of water and the measured total viscosity, $10^{-3}\ \mathrm{Pa}\cdot\mathrm{s} < \eta_s < \eta$. The microstructural contribution can then be estimated by difference, $\eta_m = \eta - \eta_s$. As will be shown in Appendix A, the precise partitioning between these two components has a negligible influence on the predicted layer geometry. In principle, however, both the solvent and microstructural viscosities in the fluid regime can be experimentally determined by performing a shear-rate sweep test and fitting the viscoelastic response with Saramito's model [40].

2.3.4. Viscosity in the solid regime - early age creep

If the solvent viscosity is assumed constant across the fluid and solid regimes, with typical fluid-state values of $10^{-3} - 10^{1}\ Pa\cdot s$, viscous dissipation in the solid state becomes negligible, and the material behaves as an almost perfectly hyperelastic neo-Hookean solid below the yield stress. This is the approach followed in the present work.

Conversely, to capture a more realistic viscoelastic response in the solid regime, for example to reproduce early-age creep [41,42], the pre-yield solvent viscosity must take significantly higher values, e.g., 10^{6}-$10^{8}\ Pa\cdot s$ [41]. This aligns with experimental observations showing that microstructural reorganization during yield transitions can cause extreme viscosity changes [43]. The pre-yield solvent viscosity can be determined via high-frequency small amplitude oscillatory shear tests [44] or creep-recovery tests [41,42]. A smooth transition between fluid and solid solvent viscosities can then be obtained using an appropriate viscosity function [43]. So, with minor adjustments, the model can also reproduce early-age creep in the solid regime following a Kelvin-Voigt viscoelastic behaviour.

3. Numerical solution

The standard approach to simulate elasto-viscoplastic flows with FEM is to formulate the problem as a monolithic system in the three primary unknown fields, namely velocity, pressure, and microstructure stress. This approach, resulting from the choice of an implicit time integration method, fully preserves the coupling between the equations, but it is computationally expensive. For this reason, the partitioned formulation proposed in [36] is here instead adopted: the mass continuity and the momentum equations are solved jointly implicitly, accounting for the elasto-viscoplastic contributions as equivalent external forces, while the constitutive law is solved separately and explicitly in the Gauss points by means of a sub-stepping algorithm. Coupling is achieved with an iterative solution scheme. Moreover, to ensure the momentum equation remains sufficiently elliptic even when the solvent viscosity is absent or very small, the Both Sides Diffusion (BSD) stabilization [45] is applied.

3.1. Discretization of momentum and mass balance

3.1.1. Weak forms and stabilizations

Following the standard Galerkin formulation, the spaces on Ω_t are defined as follows: the velocity trial space $S^u = \{\mathbf{u} \in H^1(\Omega_t) \mid \mathbf{u} = \bar{\mathbf{u}} \text{ on } \Gamma_D\}$ with corresponding test space $S_0^u = \{\mathbf{w} \in H^1(\Omega_t) \mid \mathbf{w} = \mathbf{0} \text{ on } \Gamma_D\}$, and the pressure trial and test space $S^p = L^2(\Omega_t)$, where $H^1(\Omega_t)$ and $L^2(\Omega_t)$ denote the standard Sobolev spaces [25]. The weak formulation is obtained by multiplying the momentum and mass balance equations, (1)-(2), by the respective test functions $\boldsymbol{w} \in S_0^u$ and $q \in S^p$, and integrating over the computational domain Ω_t, leading to the problem of finding $\boldsymbol{u} \in S^u$ and $p \in S^p$ that satisfy:

$$\int_{\Omega_t} \boldsymbol{w}\cdot\rho\frac{d\boldsymbol{u}}{dt}d\Omega_t = \int_{\Omega_t} \boldsymbol{w}\cdot\left(\nabla_{\boldsymbol{x}}\cdot\left(-p\boldsymbol{I} + 2\eta_s\dot{\boldsymbol{\epsilon}} + \boldsymbol{\tau}_m\right) + \rho\boldsymbol{b}\right)d\Omega_t \quad \forall\, \boldsymbol{w} \in S_0^u, \tag{22}$$

$$\int_{\Omega_t} q\left(\nabla_{\boldsymbol{x}}\cdot\boldsymbol{u}\right)d\Omega_t = 0 \quad \forall\, q \in S^p. \tag{23}$$

The domain Ω_t is discretized using first-order finite elements (tetrahedra in 3D) for both velocity and pressure fields, a standard choice in PFEM that avoids re-mapping of the primary quantities during remeshing operations [46]. However, this formulation

does not satisfy the Ladyzhenskaya-Babuška-Brezzi (LBB) condition [47]. To address this limitation, the Pressure-Stabilizing Petrov-Galerkin (PSPG) formulation [48] is employed, introducing additional stabilization terms in the weak form of the mass conservation equation.

$$\int_{\Omega_t} q\left(\nabla_{\boldsymbol{x}} \cdot \boldsymbol{u}\right)\, d\Omega_t - \sum_{e=1}^{n_e} \tau^e_{\mathrm{PSPG}} \int_{\Omega_{e,t}} \frac{\nabla q_e}{\rho} \cdot \left(\nabla_{\boldsymbol{x}} \cdot \boldsymbol{\sigma}_e + \rho \boldsymbol{b}_e - \rho \frac{d\boldsymbol{u}_e}{dt}\right) d\Omega_{e,t} = 0 \quad \forall\, q \in S^p. \tag{24}$$

Following [49] the stabilization parameter τ^e_{PSPG} can be computed for each element as:

$$\tau^e_{\mathrm{PSPG}} = \left(\left(\frac{2}{\Delta t}\right)^2 + \left(\frac{2\,\|\mathbf{u}_e\|_E}{h_e}\right)^2 + 9\left(\frac{4\eta^*_e}{\rho h_e^2}\right)^2 \right)^{-\frac{1}{2}}, \tag{25}$$

where h_e is the characteristic element size, defined as the diameter of a sphere having the same volume as the tetrahedral element; $\|\mathbf{u}\|_E$ is a local velocity scale, computed as the Euclidean norm of the velocity at the element centroid; and $\eta^*_e = \eta_s + \eta_{e,bsd}$, with η_{bsd} defined in the following, represents a local viscosity.

Alongside the PSPG formulation, it is also necessary to introduce a stabilization term in the momentum equation to address the loss of ellipticity caused by very small or vanishing solvent viscosities combined with high elastic stresses. To this end, the Both-Sides Diffusion (BSD) stabilization [45] is implemented. The idea behind the BSD method is to add an artificial diffusion term on both sides of the momentum equation, leading to:

$$\int_{\Omega_t} \boldsymbol{w} \cdot \rho \frac{d\boldsymbol{u}}{dt} d\Omega_t = \int_{\Omega_t} \boldsymbol{w} \cdot \left(\nabla_{\boldsymbol{x}} \cdot \left(-p\boldsymbol{I} + (2(\eta_s + \eta_{bsd})\dot{\boldsymbol{\epsilon}} + (\boldsymbol{\tau}_m - 2\eta_{bsd}\dot{\boldsymbol{\epsilon}}\right) + \rho \boldsymbol{b}\right)\, d\Omega_t \quad \forall\, \boldsymbol{w} \in S^u_0, \tag{26}$$

where η_{bsd} is the artificial diffusion viscosity introduced by the BSD scheme. For the proposed model η_{bsd} must be evaluated on each finite element according to the following expression:

$$\eta_{e,bsd} = \min\left(\eta_{\text{cut-off}}, \frac{\eta_m}{\beta_{fs}(t)}\right), \tag{27}$$

where $\eta_{\text{cut-off}}$ is introduced to prevent excessively high values [36].

3.1.2. Space discretization

The approximate solutions are sought in the discrete spaces $S^v_h \subset S^u$ and $S^p_h \subset S^p$, where the velocity and pressure fields are expressed in each finite element as interpolations of their respective nodal values:

$$u^i_e(\boldsymbol{x}, t) = \sum_{a=1}^{n_e} N^u_a(\boldsymbol{x}) U^i_{e,a}(t), \qquad p_e(\boldsymbol{x}, t) = \sum_{a=1}^{n_e} N^p_a(\boldsymbol{x}) P_{e,a}(t), \tag{28}$$

where n_e is the number of nodes in the element, $\boldsymbol{U}^i_e$ is the elementary vector of nodal velocities in the i-th direction, $\boldsymbol{P}_e$ is the elementary vector of the nodal pressures and N^u_a, N^p_a are the element shape functions for the velocity and the pressure respectively. The following semi-discretized in space equations are obtained:

$$\boldsymbol{M}_u \frac{d\boldsymbol{U}}{dt} + \boldsymbol{K}^* \boldsymbol{U} = \boldsymbol{F}_{ext} - \boldsymbol{F}_{evp} + \boldsymbol{F}_{bsd} + \boldsymbol{D}^T \boldsymbol{P}, \tag{29}$$

$$\boldsymbol{D}\boldsymbol{U} + \boldsymbol{L}\boldsymbol{P} + \boldsymbol{C}\frac{d\boldsymbol{U}}{dt} - \boldsymbol{H} = \boldsymbol{0}, \tag{30}$$

where $\boldsymbol{M}_u$ is the velocity mass matrix, $\boldsymbol{K}^*$ is the modified deviatoric stiffness matrix to include BSD stabilizing terms, $\boldsymbol{F}_{ext}$ is the vectors of the external forces, $\boldsymbol{F}_{evp}$ is the vector of the equivalent elasto-viscoplastic forces, $\boldsymbol{F}_{bsd}$ are the equivalent BSD forces which preserve consistency, $\boldsymbol{D}$ is the discrete divergence operator matrix, $\boldsymbol{L}$ is the PSPG Laplacian matrix and $\boldsymbol{C}$ and $\boldsymbol{H}$ are respectively a global matrix and vector, associated to the PSPG terms providing consistency. A detailed description of these terms and their derivation can be found in [36].

3.1.3. Time integration

Time discretization is performed by dividing the simulation time history into constant steps Δt and applying an implicit backward Euler scheme for the time derivatives. The resulting nonlinear equations are linearized and solved iteratively using a Picard procedure. At each time step t_{n+1} and iteration $k+1$, the updated velocities $\boldsymbol{U}^{k+1}_{n+1}$ and pressures $\boldsymbol{P}^{k+1}_{n+1}$ are obtained by solving the following strongly coupled linear system:

$$\begin{cases} \left(\frac{\boldsymbol{M}^k_{u,n+1}}{\Delta t} + \boldsymbol{K}^{*,k}_{n+1}\right)\boldsymbol{U}^{k+1}_{n+1} - \boldsymbol{D}^{T,k}_{n+1}\boldsymbol{P}^{k+1}_{n+1} = \left(\boldsymbol{F}_{ext} - \boldsymbol{F}_{evp} + \boldsymbol{F}_{bsd}\right)^k_{n+1} - \frac{\boldsymbol{M}^k_{u,n+1}}{\Delta t}\boldsymbol{U}_n, \\ \boldsymbol{L}^k_{n+1}\boldsymbol{P}^{k+1}_{n+1} + \left(\boldsymbol{D}^k_{n+1} + \frac{\boldsymbol{C}^k_{n+1}}{\Delta t}\right)\boldsymbol{U}^{k+1}_{n+1} = \frac{\boldsymbol{C}^k_{n+1}}{\Delta t}\boldsymbol{U}_n + \boldsymbol{H}^k_{n+1}. \end{cases} \tag{31}$$

3.2. Discretization of the elasto-viscoplastic constitutive law

Using the definition of upper convective derivative (12), and recalling that the convective term vanishes in a Lagrangian framework, the constitutive equation becomes:

$$\frac{\partial \boldsymbol{\tau}_m}{\partial t} - \boldsymbol{\tau}_m \cdot \nabla \boldsymbol{u} - (\nabla \boldsymbol{u})^T \cdot \boldsymbol{\tau}_m + \frac{\beta_{fs}(t)}{\lambda(t)} \boldsymbol{\tau}_m = 2G(t)\dot{\boldsymbol{\epsilon}}, \tag{32}$$

This equation represents a linear system of ODEs, which can be integrated explicitly with the forward Euler scheme and solved for the updated microstructural stress tensor $\boldsymbol{\tau}_m^{n+1}$:

$$\boldsymbol{\tau}_m^{n+1} = \boldsymbol{\tau}_m^n + \Delta t \left(\boldsymbol{\tau}_m^n \cdot \nabla \boldsymbol{u}^n + (\nabla \boldsymbol{u}^n)^T \cdot \boldsymbol{\tau}_m^n - \frac{\beta_{fs}(t_n)}{\lambda(t_n)} \boldsymbol{\tau}_m^n + 2G(t_n)\dot{\boldsymbol{\epsilon}}^n \right). \tag{33}$$

Since the explicit scheme is conditionally stable, according [36], the following conservative stability condition must be respected:

$$\Delta t_{stab} < \frac{2\eta_m}{G(t)\beta_{fs}(t)} \leq \frac{2\eta_m}{G(t)}, \tag{34}$$

where $\beta_{fs}(t) \in [0, 1]$, and thus the most conservative scenario corresponds to $\beta_{fs} = 1$.

3.3. Complete partitioned solution algorithm

At each global time step, the solution is computed through an iterative procedure: first, system (31) is solved to obtain the velocity field; this velocity is then passed to the constitutive law, which is solved to update the material response; finally, the resulting equivalent elasto-plastic forces are fed back into the momentum equation. Since to integrate the constitutive law an explicit scheme is employed, it is generally not possible to directly advance it over the entire global time step. Therefore, to ensure that the stability condition (34) is always satisfied, while retaining a large global time step for the solution of the balance equations, an adaptive sub-stepping scheme is introduced. For each element, at every iteration, the stable time increment Δt_{stab} for the constitutive integration is computed from (34), and the required number of sub-steps is determined as:

$$n_{sub} = \lceil \Delta t / \Delta t_{stab} \rceil, \tag{35}$$

where $\lceil \bullet \rceil$ denotes the ceiling operator, and Δt is the global time step used for the implicit integration of the balance equations. The detailed implementation of the sub-stepping algorithm can be found in [36]; only the final solver procedure is summarized in Algorithm 1.

Algorithm 1 Elasto-viscoplastic partitioned solver.

```
while (t < t_f) do
    while (err_v > tol_v or err_p > tol_p) do
        Solve the linearised balance eqs. (31) implicitly
        for j = 1, n_sub do
            Solve the constitutive law (33) explicitly
        end for
        Update coordinates: x_{n+1}^{k+1} = x_n + U_{n+1}^{k+1} Δt
        k = k + 1
    end while
    t_{n+1} = t_n + Δt
end while
```

The efficiency of the algorithm is ensured by the fact that the solution of the constitutive law, which must be computed multiple times due to sub-stepping, requires only scalar operations performed locally on each finite element. To further mitigate the computational cost associated with solving the monolithic implicit system of the balance equations, the linear system is solved using an in-house Fortran code optimized for performance, leveraging Intel® oneAPI Math Kernel Library (oneMKL) tools for sparse CSR matrix and vector operations, and the PARDISO MKL direct solver for the system solution.

3.4. Overview of the Particle Finite Element Method (PFEM)

The use of a Lagrangian framework across most of the computational domain offers several advantages, including the inherent ability to capture free surfaces and the elimination of nonlinear convective terms from the momentum and constitutive equations. However, since nodal positions are updated based on the computed velocity, problems involving large displacements and deformations can cause the deterioration of the computational mesh. If a proper strategy is not used to cure the problem, accuracy and stability issues can arise, even preventing the possibility of computing a solution.

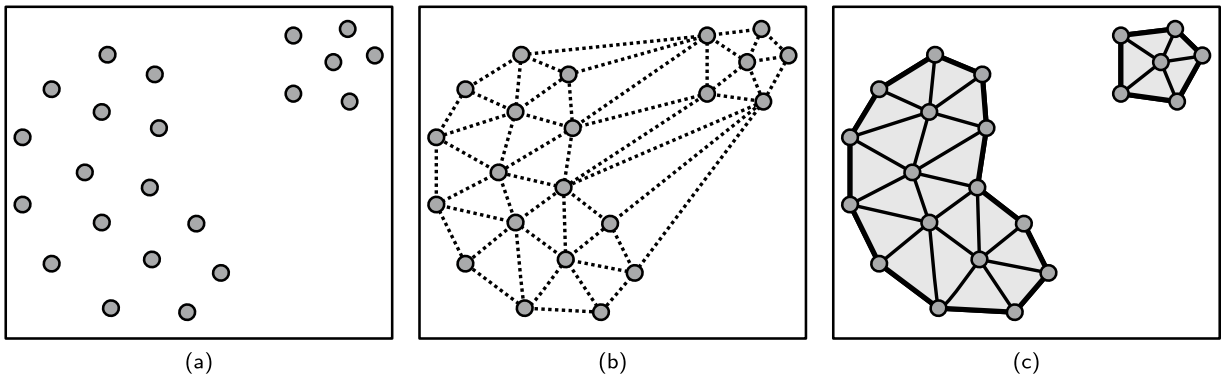

Fig. 2. Re-meshing scheme in PFEM: initial point cloud (a); Delaunay triangulation convex hull (b); final mesh with the identified free-surface after application of the α-shape method (c).

A possible remedy is offered by the Particle Finite Element Method (PFEM) [46,50], which enhances the updated Lagrangian approach with an efficient remeshing strategy. Originally developed for the simulation of free-surface flows and breaking-wave phenomena [50], PFEM has been successfully extended to a wide range of engineering applications, including fluid-structure interaction [51,52], complex flows [36,53–55], and industrial forming processes [56,57].

More recently, PFEM has emerged as an ideal framework for additive manufacturing simulations, thanks to its intrinsic ability to handle evolving interfaces, contact interactions, and multi-physics coupling. It has been effectively employed to reproduce extrusion and layer deposition in 3D printing with cementitious materials [16–18] as well as melt-pool dynamics in metal deposition [58,59].

The underlying idea in the PFEM is to adopt a re-meshing scheme to create a new mesh whenever the existing one becomes excessively distorted. The key steps of the re-meshing process are explained in Fig. 2. Throughout the analysis, the mesh quality is monitored, and, whenever distortions become excessive, the mesh is deleted, preserving only the nodes, as shown in Fig. 2-a. Then, a new connectivity is generated with an efficient tool such as the Delaunay algorithm [60] (Fig. 2-b). Finally, the "α-shape method" [61] is applied to isolate the physical boundaries and determine the free surface (Fig. 2-c). Practically, this is done by removing those elements that are greatly distorted and thus are less likely to belong to the fluid domain. For further details on the PFEM approach the reader is referred to [46,50].

3.5. Transfer of historical variables in PFEM

As previously illustrated, PFEM can handle large deformation problems in solid mechanics as well as the simulation of fluids with complex rheology. Such materials often involve constitutive laws that depend on historical variables, such as elastic stresses or internal state variables. When standard Gaussian integration is used, these variables may be lost after remeshing unless an appropriate transfer procedure is applied.

A commonly used and straightforward approach is nodal-based mapping, where historical variables are first mapped to the nodes before remeshing and then recovered at the new Gauss points via shape function interpolation. However, this procedure can lead to excessive smoothing of internal variables, potentially affecting the accuracy of the solution. To address the issue, in this work we adopt the method proposed in [36,53,62], in which only the increments of historical variables are mapped to the nodes at each time step to reduce the smoothing effect. Moreover, the reverse mapping from nodes to Gauss points is performed only when a remeshing event occurs, further minimizing errors.

It is worth noting that the reverse mapping procedure can also be applied, for a different purpose, to quantities defined intrinsically at the nodes - such as temperature or pressure - that enter the constitutive law. In these cases, shape functions are used to extrapolate their values to the Gauss points, and no back-transfer to the nodes is needed, since the constitutive update does not alter the nodal values.

3.6. Computational strategies for reproducing 3D printing in PFEM

PFEM provides a versatile and robust framework, well-suited for modelling both the flow of complex fluids and large deformations in solids, making it a promising approach for the unified simulation of 3D printing across process scales. To achieve this, however, it must be complemented with a set of *ad hoc* techniques specifically designed to capture the complex, time-dependent boundary conditions characteristic of material extrusion and layer deposition processes. These techniques, introduced in our previous works [17,18], are briefly reviewed below, and we show how they remain valid and applicable here despite substantial differences in the finite element solver.

3.6.1. Arbitrary nozzle movements and continuous material flow

In 3D printing processes the nozzle will translate and rotate in space according to some user-defined instructions, generally specified by the *G*-code. To facilitate the imposition of moving boundary conditions at the virtual nozzle outlet, it was proposed in [17] to formulate the governing equations within the ALE framework.

The key idea of the ALE is to decouple the movement of the computational mesh from the physical movement of the material particles. In particular, this fact can be exploited to assign different mesh velocities $\boldsymbol{v}$ to different portions of the domain. The discrete boundary at the nozzle outlet will be assigned a mesh velocity equal to the printing velocity $\boldsymbol{v} = \boldsymbol{v}_p$, while the remaining nodes of the computational domain are instead always treated in a standard Lagrangian fashion, by prescribing a mesh velocity coincident with the physical velocity $\boldsymbol{v} = \boldsymbol{u}$, as shown in Fig. 3. The mesh velocity is then used at each time step to update the position of the generic node i:

$$\boldsymbol{x}_i^{t+1} = \boldsymbol{x}_i^t + \boldsymbol{v}_i^t \Delta t. \tag{36}$$

By modelling arbitrary nozzle translations prescribing the mesh velocity, it is possible to assign to the ALE nodes at the nozzle outlet the inflow velocity $\boldsymbol{u} = \boldsymbol{u}_f$ as a standard Dirichlet boundary condition. In fact, because their position update is based solely on mesh velocities, these nodes do not flow downward, but instead transmit by means of convection the inflow velocity to the adjacent Lagrangian nodes.

Over time, Lagrangian nodes near the inflow boundary will move downward, leading to mesh stretching. To mitigate this issue, new nodes are inserted and re-meshing is performed in the computational domain whenever these elements become overly stretched (see Fig. 3). This ensures a continuous material flow out of the nozzle.

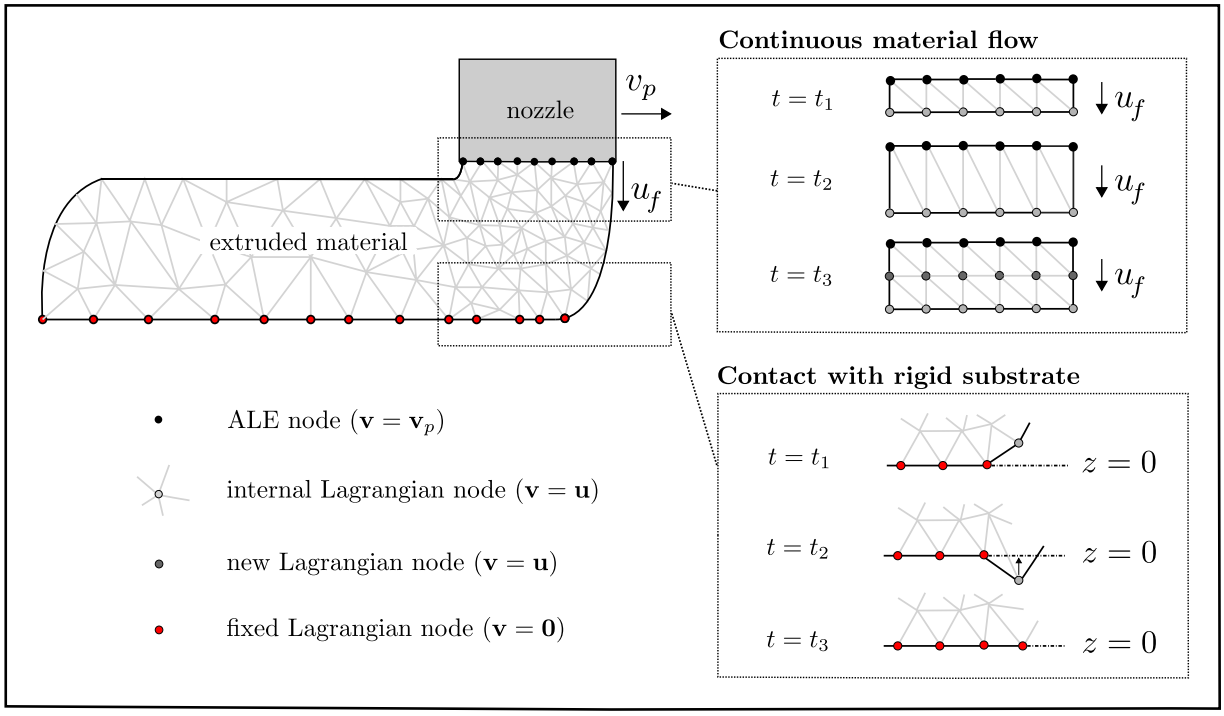

Fig. 3. Computational strategies adopted in the PFEM to reproduce the continuous material flow out of the nozzle and the contact with the rigid substrate.

3.6.2. Rigid print bed and interlayer contact

The contact strategy, first introduced in [17] to minimize spurious volume variations due to remeshing and the α-shape criterion [63] during the interaction between the extruded material and the print bed is here extended. Specifically, Dirichlet boundary conditions (DBCs) are imposed by "freezing" (setting the velocity to zero) nodes that satisfy a prescribed positional constraint. To illustrate, consider the simplest case of a planar horizontal print bed, defined by $z = 0$ and shown in Fig. 3. During the simulation, the z-coordinates of the free Lagrangian nodes are monitored, and whenever a node i satisfies $z_i \leq 0$, it is projected back onto the $z = 0$ plane and the DBC $\boldsymbol{u}_i = \mathbf{0}$ is strongly enforced to replicate contact with the plane. Note that in [17] the projection step was absent; the use of an explicit integration scheme, necessitating very small time steps, automatically ensured accurate contact enforcement. Here, due to implicit time integration, potential errors are larger, and the projection step improves adherence to the boundary condition.

An interlayer contact strategy is also proposed, generalizing the algorithm in [17] to enable smooth merging between adjacent layers. Compared to the standard PFEM merging mechanism [63], this approach allows better control of artificial volume variations

and maintains consistency even with relatively coarse mesh resolutions. In PFEM, the free surface is identified after each remeshing using the α-shape criterion. Building on this, the contact strategy modifies the α-shape procedure to remove elements that are entirely part of the free surface (i.e., elements whose nodes are all free-surface nodes), preventing automatic merging of layers that would otherwise produce non-physical volume increase. A second criterion enforces controlled contact based on the distance between free-surface nodes: whenever two nodes are closer than a prescribed threshold, one is deleted and a remeshing operation is triggered, effectively achieving local merging of the two layers, as illustrated in Fig. 4. With respect to [17] the present method is slightly more general, as it does not rely on free-surface refinement or internal near-free-surface derefinement to achieve effective interlayer contact, resulting in virtually no additional computational cost compared to standard PFEM operations.

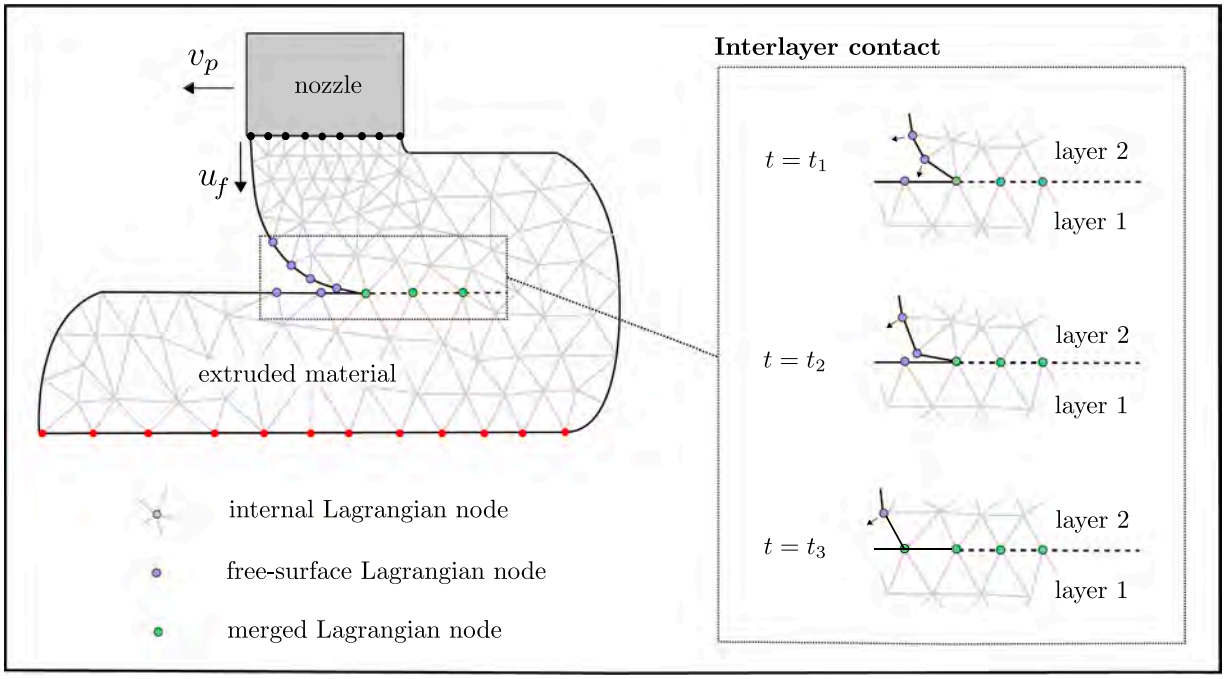

Fig. 4. Computational strategies adopted in the PFEM to reproduce interlayer contact.

4. Results

The numerical framework is validated against a series of 3D printing experiments conducted using the large-scale 3D concrete printing facility at Eindhoven University of Technology (TU/e), encompassing scenarios with different spatial and temporal scales. The first section focuses on the simulation of straight and inclined walls printed with a single filament width, while the second addresses the virtual printing of a more complex structural component. Prior to discussing these applications, the materials and 3D printing setup used at TU/e are presented.

4.1. Material properties and mechanical characterization

The cementitious mortar used in the printing process (Weber 160-2) consists of Portland cement, aggregates (maximum size 4 mm), limestone, non-structural polypropylene fibers for early age crack control, and admixtures to improve workability and extrudability. The average density was estimated to be $\rho = 2316\ kg/m^3$. Uniaxial Unconfined Compression Tests (UUCTs) were conducted on cylindrical specimens to obtain the material's stress-strain response at 5, 15, 30, 60, and 90 minutes after extrusion from the 3D printer. To ensure homogeneity and a representative material state compared to the printing process, the samples were filled by directly extruding the mortar into the moulds, without any additional compaction. For each age at least four nominally identical specimens were tested using an Instron test rig. As detailed in Appendix A, the Young's modulus (E) and the compressive strength (σ_c) were extracted from each stress–strain curve. Owing to their clearly exponential trend, the results were modeled using an exponential function of the form $Ae^{Bt} + C$, with parameters estimated by nonlinear least-squares regression. Fig. 5-a shows the mean Young's modulus and its regression curve over specimen age. Fig. 5-b presents the compressive yield strength data and the fitted curves for the mean, minimum, and maximum values at each age.

The Poisson's ratio was estimated from lateral expansion measurements and used solely to compute the time-dependent shear modulus $G(t)$ from the elastic modulus $E(t)$. From the time evolution of the compressive yield strength $\sigma_c(t)$, the corresponding von Mises yield stress $\tau_{0,VM}(t)$ can be directly derived or, alternatively, the cohesion $c(t)$ can be obtained once the friction angle

ϕ is determined [39] (see Appendix A for further details). Subsequently, the friction angle and cohesion are converted into the Drucker–Prager parameters $k(t)$ and α using equations (16, 17). Table 1 reports the initial values (at $t = 0$) of all parameters, while the full exponential time-evolution expressions for the time-dependent quantities - namely the shear modulus, the yield stress, and the cohesion-related Drucker–Prager parameter - are provided in Appendix A.

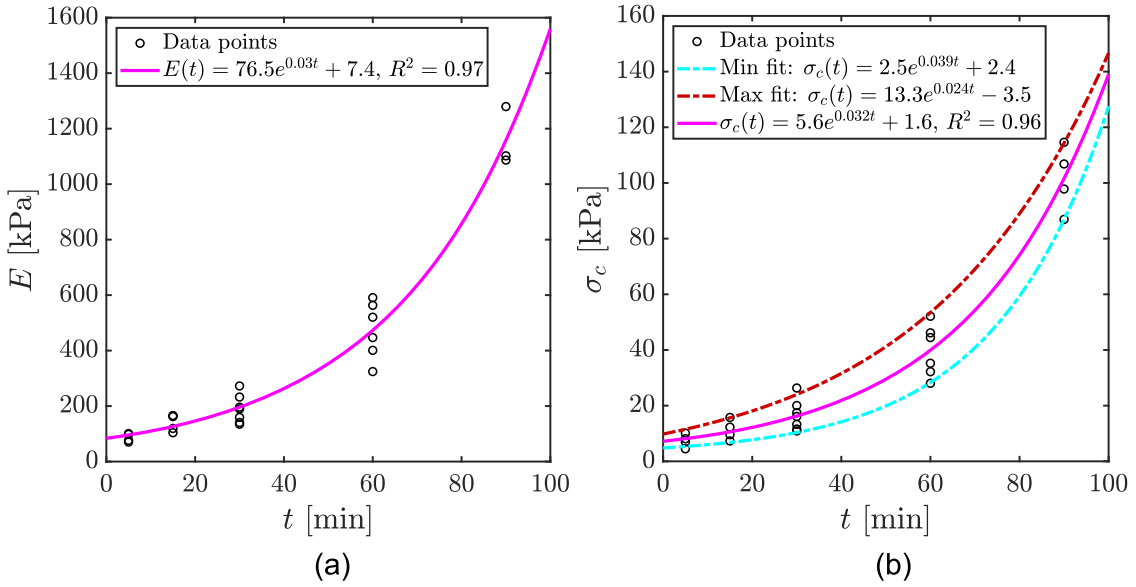

Fig. 5. Elastic modulus (a) and compressive yield strength (b) evolution with specimen age (t) as obtained from UUCTs.

Table 1
Material properties.

Material model	ρ [kg/m^3]	$\tau_{0,VM}(t=0)$ [Pa]	$k(t=0)$ [Pa]	α [–]	$G(t=0)$ [Pa]	η_s [Pa·s]	η_m [Pa·s]
Bingham	2316	4158	–	–	–	10	–
Saramito	2316	4158	–	–	32 260	1	9
Saramito-DP	2316	–	3088	0.446	32 260	1	9
Saramito-DP max	2316	–	4202	0.446	32 260	1	9

4.2. 3D printing setup and process parameters

All printing experiments were performed using the 3D concrete printing setup of TU/e, which consists of a large-scale gantry robot coupled with a MAI®MULTIMIX-3D mixer-pump. The pre-mixed dry material is stored in a silo and mixed with water at a ratio of approximately 10% by mass. Then, the material is pumped over about 15 m distance to the print head, which contains a conical nozzle with an opening of 25 mm.

A layer-pressing printing strategy was employed in all cases, as this approach improves inter-layer adhesion and achieves more constant layer's heights, thereby reducing uncertainties in the geometry of the final object. To achieve the layer-pressing flow regime, a nozzle height of $h_n = 12.5$ mm was selected, which is smaller than the nozzle diameter $\phi_n = 25$ mm. This was combined with a flow rate exceeding the print speed, so that each extruded layer is slightly compressed against the previous one. For 3D printing of the wall, the parameters listed in the second column of Table 2 were used, whereas those reported in the third column of the same table were applied when printing the V-shaped structural component (V-object).

Table 2
Printing parameters.

Printing parameters	Walls	V-object
Nozzle diameter (ϕ_n)	25 mm	25 mm
Nozzle height (h_n)	12.5 mm	12.5 mm
Print velocity (v_p)	91.7 mm/s	87 mm/s
Flow velocity (u_f)	95 mm/s	100 mm/s

4.3. 3D printing vertical and inclined walls

This section examines the virtual printing of multilayer rectilinear walls with vertical and inclined geometries. The walls have a length of $l = 500\,\text{mm}$ and out-of-plane inclination angles $\gamma = 0°, 1°, 2°, 5°$, and $10°$, as shown in Fig. 6. Successive layers are offset by $\Delta z = h_n = 12.5\,\text{mm}$ in the vertical direction and by $\Delta y = \Delta z \tan\gamma$ in-plane. The corresponding nozzle displacements are applied progressively, starting $50\,\text{mm}$ before the filament end to ensure a smooth transition. Moreover, to limit boundary effects and stabilize the extrusion process, the first layer begins $100\,\text{mm}$ upstream of the wall. Each configuration was printed three times to reduce experimental variability.

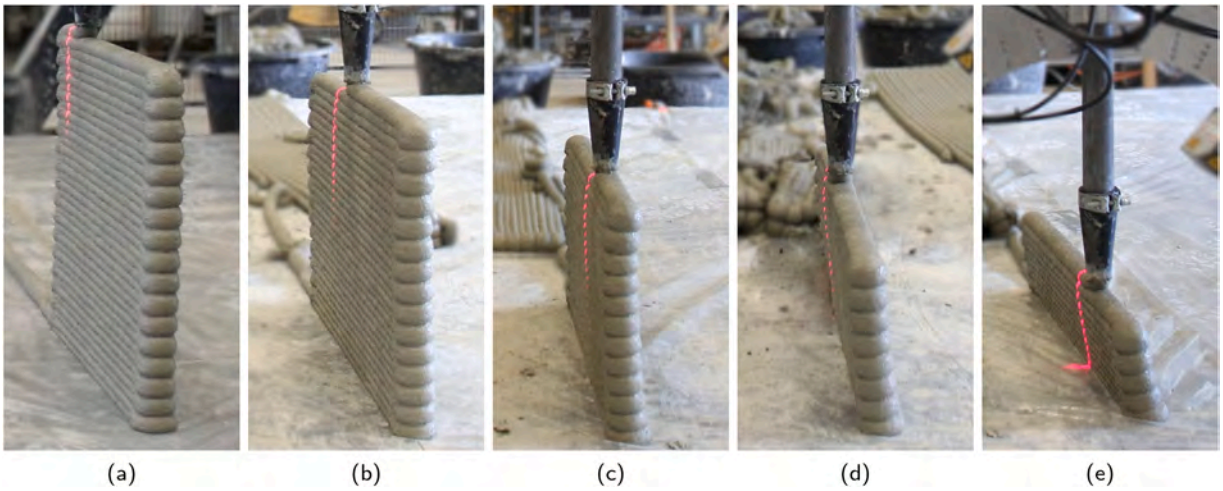

Fig. 6. 3D-printed walls with out-of-plane inclination angles of 0° (a), 1° (b), 2° (c), 5° (d), and 10° (e), shown during the final phase of the printing process, close to collapse.

Fig. 6 also shows the presence of two *scanCONTROL 2900–100* laser scanners positioned immediately behind the nozzle, each capturing data from one side of the wall. This configuration enables accurate reconstruction of the cross-sectional profiles [64], which are then used for comparison with the numerical results. In the following, since the profiles extracted from the three repetitions of the printed walls were nearly identical - even when taken at different positions along the wall - only the laser-scanned profiles from a generic representative case will be shown. Particularly, for this representative case experimental profiles are extracted at midspan, after the completion of each odd-numbered layer.

4.3.1. 3D printed walls: validation at the scale of the filaments

As a starting point, the simulation focused on reproducing the printing of the first layers of the walls and employed a fine mesh with an average element size of $h_e = 2\,\text{mm}$. With about ten elements spanning the layer width, the mesh offered sufficient resolution to capture the layer's shape with high quality.

Fig. 7 presents the results for the vertical-wall case, showing a comparison, up to the 9^{th} layer, between the experimental cross-sectional profiles of a representative wall (in black) and the numerically predicted outlines. The latter were obtained using two different constitutive models: the standard Bingham model (in blue) and the proposed *Saramito-DP* model (in red). Both models show very good overall agreement with the experiments; however, the Bingham model consistently overestimate the width of the top layers, while underestimating the total height of the walls by a couple of millimeters.

This behaviour can be understood with reference to Fig. 8. When a new layer is deposited onto the previously printed layers, the extruded material exerts a localized pressure increment on the underlying substrate, which represents the dominant loading mechanism and induces localized shear deformations beneath the nozzle. In contrast, the self-weight of the newly deposited layer constitutes a comparatively small, quasi-static load that persists after the nozzle passage. Fig. 8-b illustrates the substrate response both during and after the nozzle passage - that is, during and after the removal of the localized pressure increment - highlighting the differences in behaviour of different materials. This visualization enables a direct comparison of how the underlying layers deform under the advancing extrusion and how these deformations evolve and partially persist even once the nozzle has moved away.

For a Bingham substrate, which exhibits purely viscoplastic behaviour, the applied load induces irreversible plastic deformations that persist after the nozzle has passed. In contrast, for a purely elastic substrate, the deformation is entirely recoverable, allowing the material to return almost completely to its original configuration once the load is removed. In the case of an elasto-plastic substrate, as described by the *Saramito-DP* model, the response is spatially heterogeneous: regions in the immediate vicinity of the nozzle undergo plastic deformation, while areas farther away remain within the elastic regime. As a consequence, only part of the deformation is recovered after unloading. The substrate partially regains its original shape, leading to a vertical re-expansion that contributes to lifting the newly deposited layer and influencing its final geometry.

This elastic recovery mechanism is absent in purely viscoplastic models, thereby explaining the superior ability of the *Saramito-DP* model to accurately predict the printed geometry and associated deformations compared to the Bingham model.

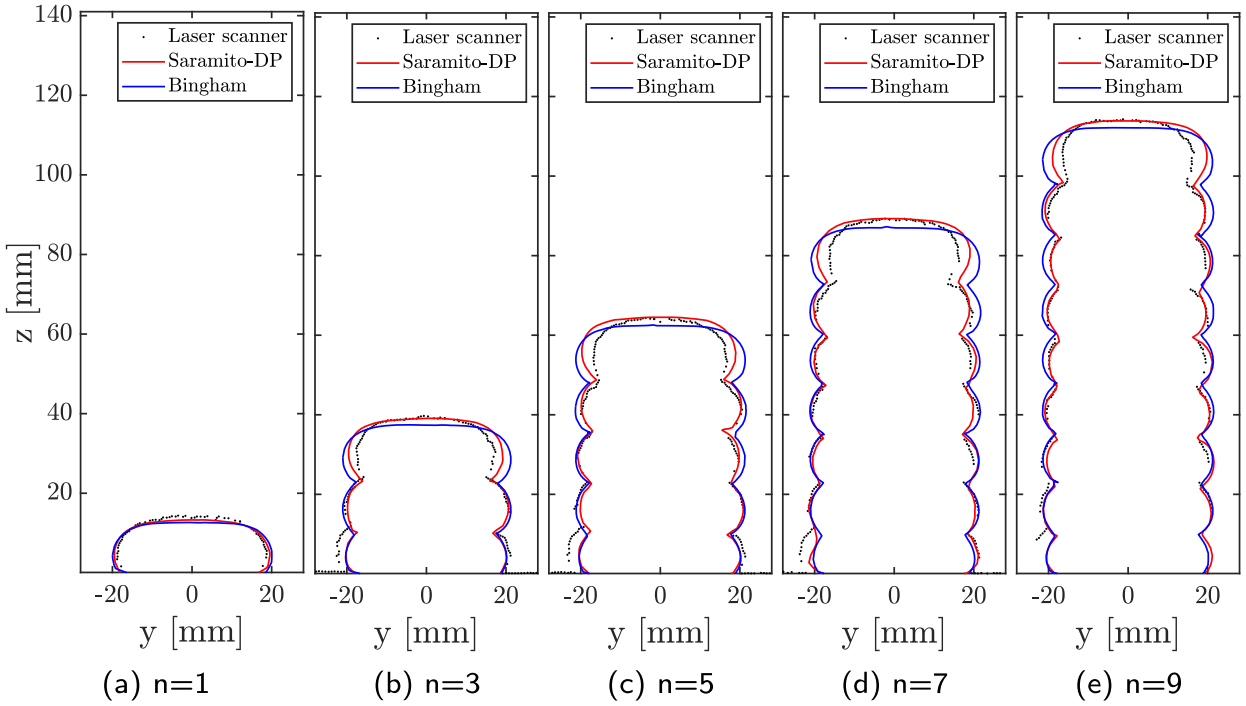

Fig. 7. Comparison between experimental and numerical cross-sections after the extrusion of layers number 1, 3, 5, 7 and 9 for the vertical wall $\gamma = 0°$.

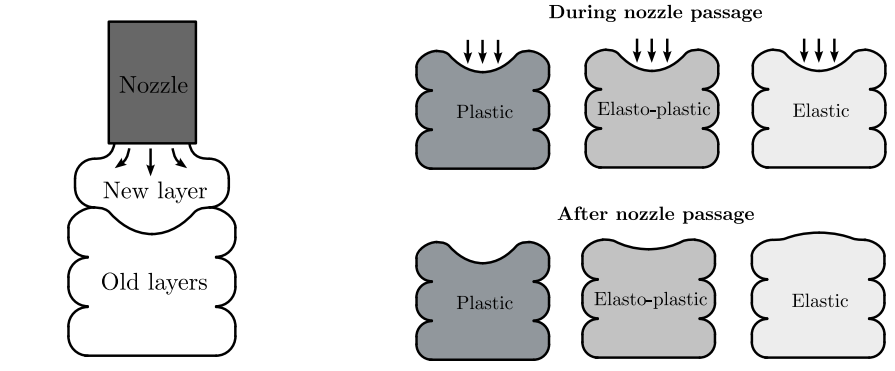

(a) Extrusion of a new layer. (b) Effect of the elasticity of the substrate.

Fig. 8. Simplified schematic illustrating the role of elasticity in defining the shape of layer's cross-sections.

Fig. 9 compares the cross-sectional profiles up to the 5th layer for the inclined walls, showing both the experimentally measured profiles and the corresponding numerical predictions obtained using the *Saramito-DP* model. It can be observed that, regardless of the wall inclination, the model accurately captures the vertical deformations and provides a good overall approximation of the full cross-sectional geometry. Notably, the material exhibits increased deformation on the inclined side, as evidenced by the less defined and more flattened layer outlines compared to the opposite side.

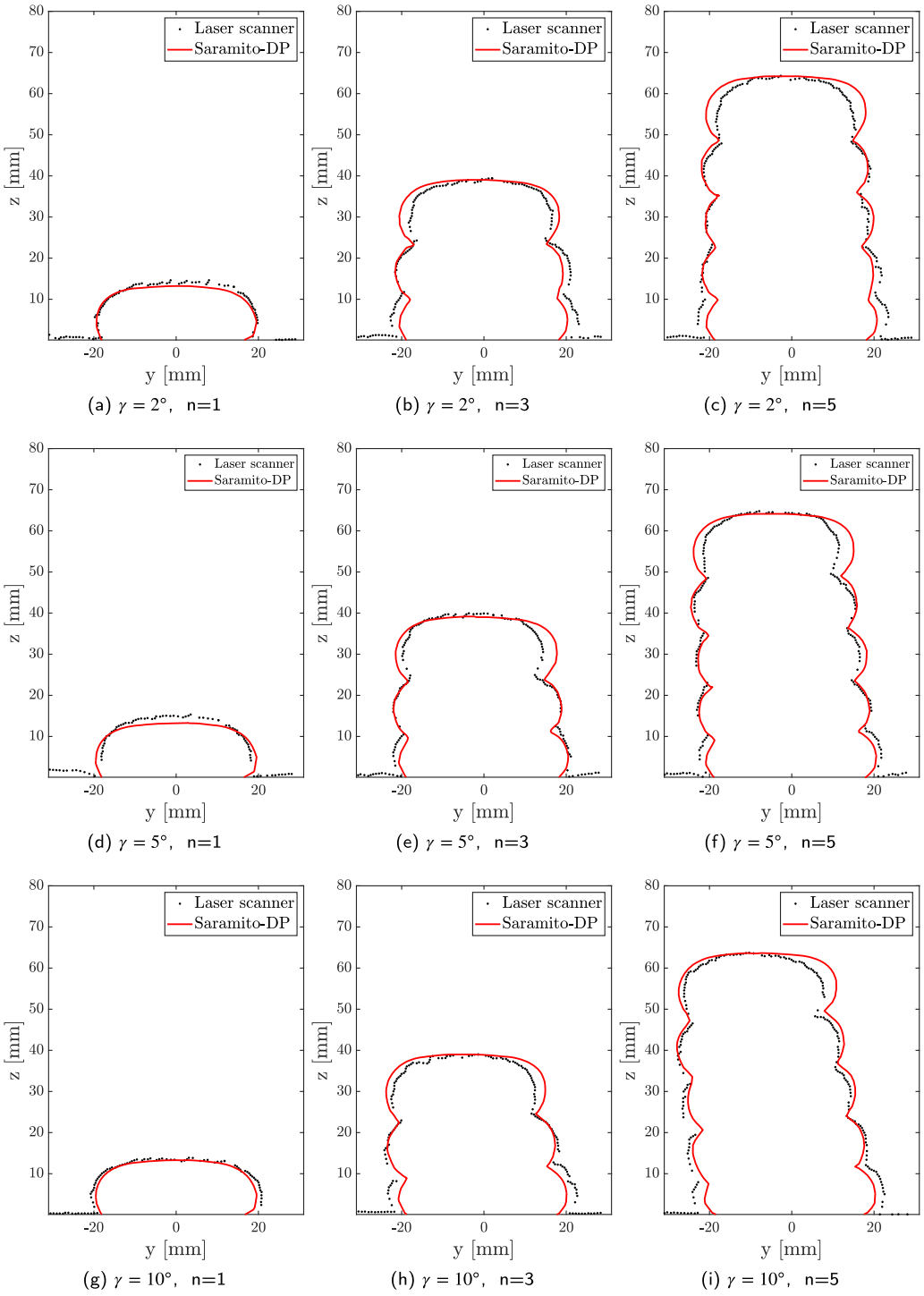

Fig. 9. Comparison between experimental and numerical cross-sections after the extrusion of layers number 1, 3 and 5 for walls inclined of 2°, 5° and 10°.

4.3.2. 3D printed walls: validation at the scale of the object

This section addresses the full printing process of the walls up to collapse. A new set of analyses was performed to simulate the complete 3D printing process for the five different wall configurations. To reduce the computational cost, only half of the wall length (250 mm) was simulated, but to maintain consistency with the experiments the time evolution of the material properties was scaled by a factor of two. This was achieved through a simple time scaling, such that the effective time is defined as $t_{\text{eff}} = 2t$. The effective time

was then used exclusively to evaluate the time-dependent mechanical properties according to the expressions reported in Appendix A, namely $E(t_{\text{eff}}) = E(2t)$, $\tau_0(t_{\text{eff}}) = \tau_0(2t)$ and $k(t_{\text{eff}}) = k(2t)$. Additionally, a slightly coarser mesh with an average element size of 3–4 mm was employed. This approach is necessary because, particularly for vertical or slightly inclined walls–where a substantial number of layers can be printed–the resulting computational domains become very large, potentially exceeding 400 000 nodes, which in turn leads to long simulation times.

Fig. 10 presents both experimental and numerical snapshots of the printing process for the vertical wall up to the point of collapse. Overall, there is good agreement between the two in terms of geometry and global deformation throughout the various stages of the printing process (Fig. 10-a-d and g-j), as well as during collapse. In particular, the model accurately reproduces the initiation of large out-of-plane displacements (Fig. 10-e) and the subsequent evolution of the overall failure mode (Fig. 10-f). These results demonstrate that the numerical framework captures not only the progressive deformation of the printed layers but also the critical mechanisms leading to structural instability.

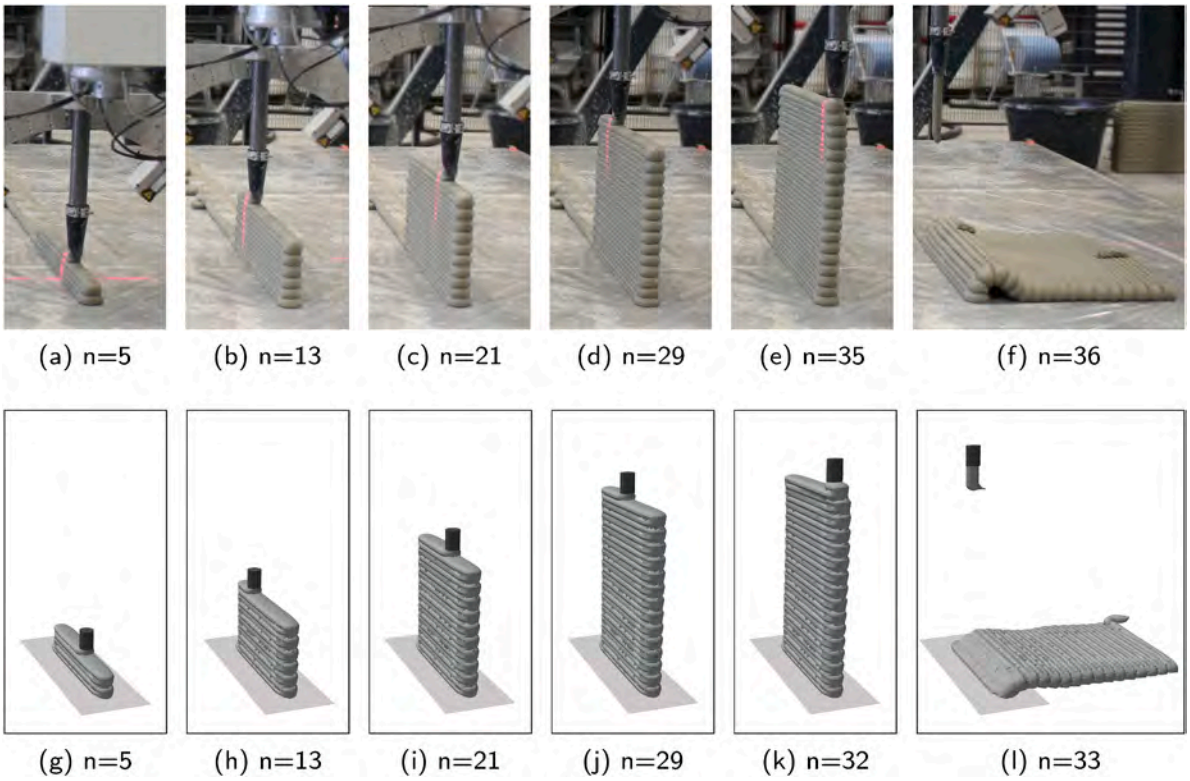

Fig. 10. Stages of the printing of the vertical wall $\gamma = 0°$ both experimentally (a-f) and numerically with *Saramito-DP max* model (g-l).

Fig. 11 illustrates the collapse mechanism in detail. Once the wall reaches a critical height, the combination of accumulated compressive stresses and geometric imperfections generates a non-negligible bending moment. This causes a slight lateral deflection of the deposited layers (Fig. 11-a), resulting in misalignment of subsequent layers with respect to the previous ones (Fig. 11-b). The offset amplifies the bending moment, progressively increasing the out-of-plane deformation. When the base of the wall undergoes plasticization (Figs. 11-c,d), the structure loses its limited out-of-plane stiffness and collapses globally (Fig. 11-e), also breaking the filament being extruded. The entire collapse process, from activation to global failure, occurs within only a few seconds.

The collapse direction of the vertical wall is governed by symmetry breaking. Although no explicit geometric imperfection was introduced in the numerical model, unavoidable numerical asymmetries act as implicit perturbations, determining both the initiation of collapse and its direction. These asymmetries arise from factors such as mesh discretization, re-meshing operations, time-integration errors or solver tolerances. Similarly, the experimental setup is subject to unavoidable imperfections - such as geometric misalignments, material heterogeneity, and nonuniform boundary conditions, so that also in practice collapse may occur to either side with comparable probability.

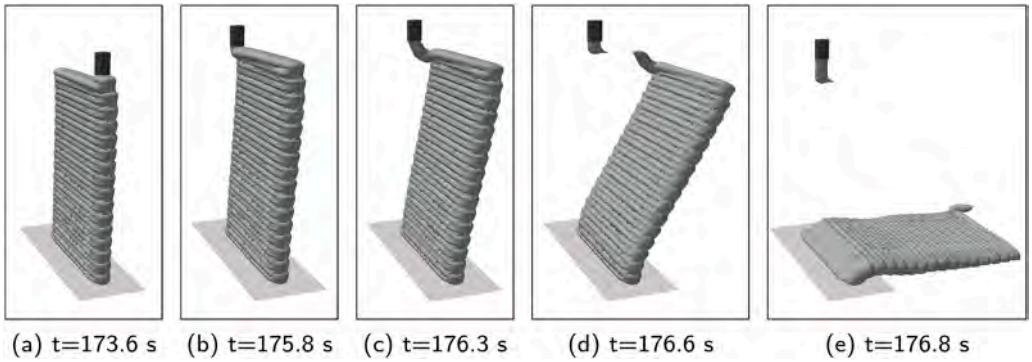

Fig. 11. Out-of-plane collapse mechanism of the vertical wall $\gamma = 0°$.

In overhanging structures, the wall inclination acts as an intrinsic imperfection that can dominate over other geometric defects and trigger instability at an earlier stage. Fig. 12 shows the virtual printing of walls inclined at 2°, 5°, and 10°. The collapse mechanism is similar in all cases, but walls with higher inclinations fail earlier.

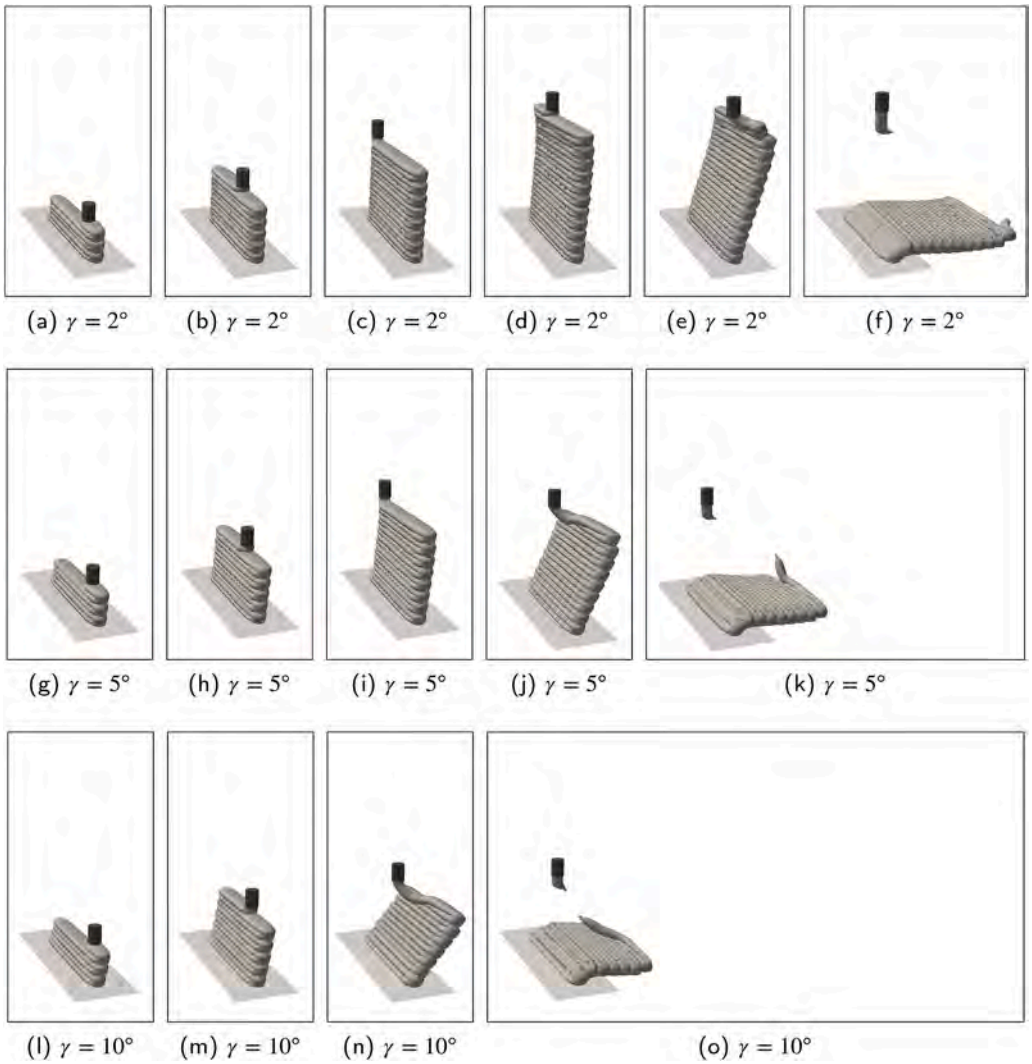

Fig. 12. Stages of the printing of the walls inclined of $\gamma = 2°,\ 5°,\ 10°$ reproduced numerically with *Saramito-DP max* model (g-l).

The complete results, expressed as the number of printed layers at collapse, are reported for both experiments and simulations in Table 3 and illustrated in Fig. 13. Here, the number of layers at collapse refers to the layer being printed when failure occurred, even if it was not fully completed. In the experiments, each wall was 3D printed three times. The rounded averages and standard deviations of the observed collapse layers are also provided.

Table 3
Number of printed layers at collapse observed in the experiments and in the simulations for rectilinear walls with different out-of-plane inclination angles (γ).

γ [°]	EXP	Saramito	Saramito-DP	Saramito-DP max
0	37 ± 2	26	29	33
1	30 ± 1	22	25	28
2	24 ± 1	20	22	24
5	18 ± 1	16	17	18
10	12 ± 0	13	14	14

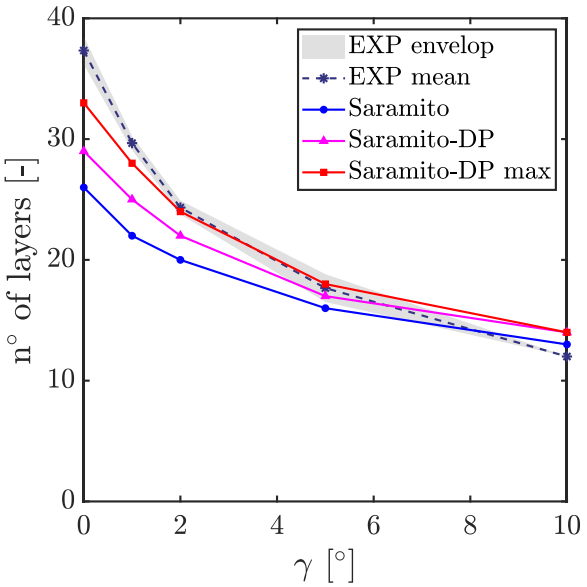

Fig. 13. Number of layers at incipient out-of-plane collapse as measured from the experiments (EXP) and as obtained from the 3D printing simulations with different constitutive laws.

Numerical simulations were carried out using the average mechanical properties, for both the standard *Saramito* model, which employs a von Mises yield criterion, and the proposed *Saramito-DP* model, which incorporates the Drucker-Prager criterion. Overall, both models exhibit a similar trend when comparing numerical predictions with experimental results. However, the comparisons indicate that accounting for frictional effects through the Drucker-Prager criterion significantly improves buildability predictions, particularly for near-vertical and vertical walls. In these cases, higher internal pressures develop, causing the yield surface to expand and better capturing the material response under confined conditions.

However, despite both models performing well for inclined walls, their predictions tend to deteriorate for progressively straighter walls. This discrepancy likely arises from two factors. First, uncertainty in the measured material properties, which can vary substantially as shown in Fig. 5, can significantly contribute to deviations. To investigate this, a third set of simulations was conducted using the *Saramito-DP max* model, i.e., for which the upper-bound compressive strength values were used to compute Drucker-Prager parameters $k(t), \alpha$. This approach improved predictions even for near-vertical walls, with deviations of only a few layers-well within the experimental uncertainty of 1-2 layers.

Nevertheless, a small but consistent underestimation of failure in straight or nearly vertical walls appears to be intrinsic to the model. This behaviour is likely related to geometrical factors: walls with minimal inclination are highly sensitive to even minor imperfections, whereas in inclined walls, the dominant imperfection is the wall's inclination itself. As a result, numerical artifacts, such as those introduced during remeshing, can generate exaggerated imperfections compared to reality, which can meaningfully

influence the onset of collapse and slightly anticipate failure. Future work will focus on reducing computational costs to enable more detailed investigations of these effects and to better quantify the role of numerical and geometric imperfections in the failure process.

4.4. 3D printing of a structural component

The final application investigates the virtual printing of an object representative of a small structural component. The object has in-plane dimensions $b = 450\,\text{mm}$ and $w = 160\,\text{mm}$, with a total height of $h = 125\,\text{mm}$, as shown in Fig. 14-a. The toolpath consists of ten layers forming a V-shaped geometry, with the corners smoothly connected by circular arcs of radius 20 mm. The material and printing parameters listed in Tables 1 and 2 respectively were adopted for the simulation. Fig. 14-b shows a snapshot of the corresponding printing process performed in the TU/e laboratory.

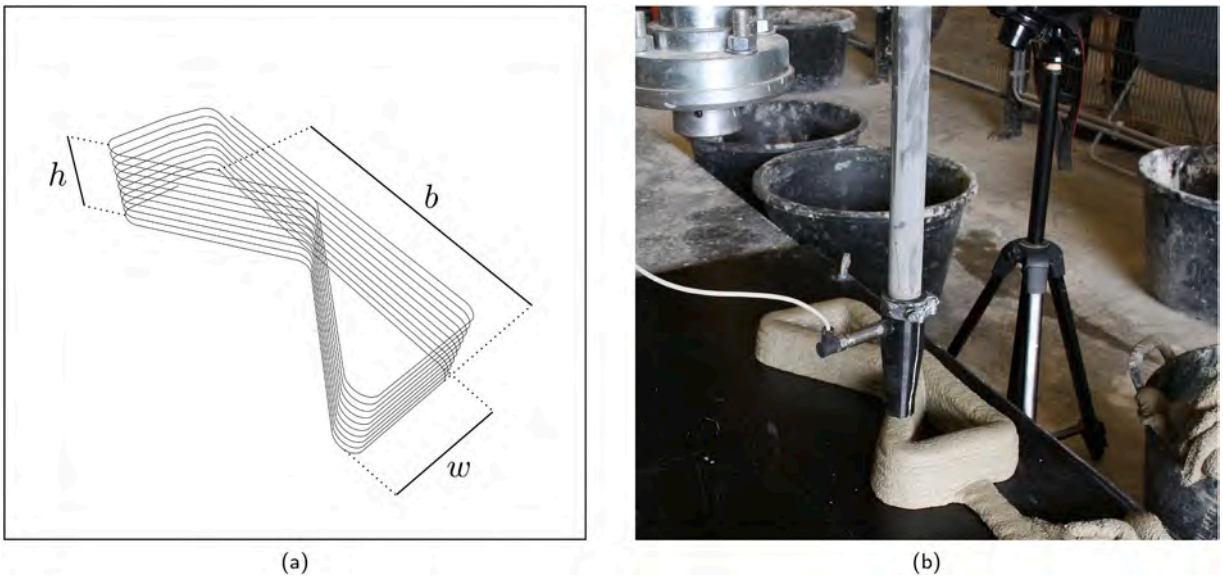

Fig. 14. Toolpath and object dimensions (a); 3D printing of the V-object (b).

The analysis simulated a total process time of approximately three minutes. The characteristic mesh size ranged between 3 and 4 mm, resulting in a discretization of about 100 000 nodes and 860 0000 elements at the end of the printing of the tenth layer. The computation required roughly ten days to complete on a 16-core 12th Gen Intel® Core™ i9-12900KF processor, employing eight cores in parallel.

Focusing on the first layer, Fig. 15 compares the actual printing process (a) with the corresponding virtual simulation (b). The results demonstrate that the unified fluid-solid modelling approach accurately captures the material distribution at corners and the merging of layers at intersections. This is particularly significant because, in practice, the size and shape of these joints, as well as the degree of overlap and interlayer contact, directly affect the mechanical strength and stiffness of the printed structure. In contrast, standard solid-based FEM models using element or layer activation often struggle to reproduce these effects and must rely on strong simplifying assumptions regarding the geometry of the layers and joints.

Fig. 16 shows a detailed view of the virtual printing process at the junction between the straight and V-shaped inclined edges, highlighting the stress norm distribution. Red regions indicate material that has yielded and behaves as a fluid, whereas the other colors correspond to regions in the phase-transitioning or solid state. A significant portion of the newly deposited filament, as well as parts of the previously printed layers, yields, ensuring strong merging and bonding between layers (Fig. 16-c,d,e). The model also captures fine details, reproducing the slight rib of material squeezed upward at the junction and the subtle bulging beyond the outer rectangle perimeter (Fig. 16-f). Both effects result from partial layer superposition and are also visible in the experimental photographs.

Finally, Fig. 17 compares the experimentally printed object (a, c) with its simulated counterpart (b, d). The numerical model accurately reproduces the overall geometry, capturing localized deformations at corners and intersections, and realistically accounting for inter-layer contact and merging both vertically and in-plane, thereby providing a reliable indication of the final object's geometrical conformity. Moreover, as shown previously, the model can predict structural collapse and, in this case, correctly indicates stability up to the 10^{th} layer. This example completes the framework validation, demonstrating how the model can predict mechanical phenomena and their impact on the printing process across multiple scales-from individual filaments to the full structural object-and across different material phases, from fluid to solid, offering a comprehensive unified framework for simulating 3D printing with cementitious materials.

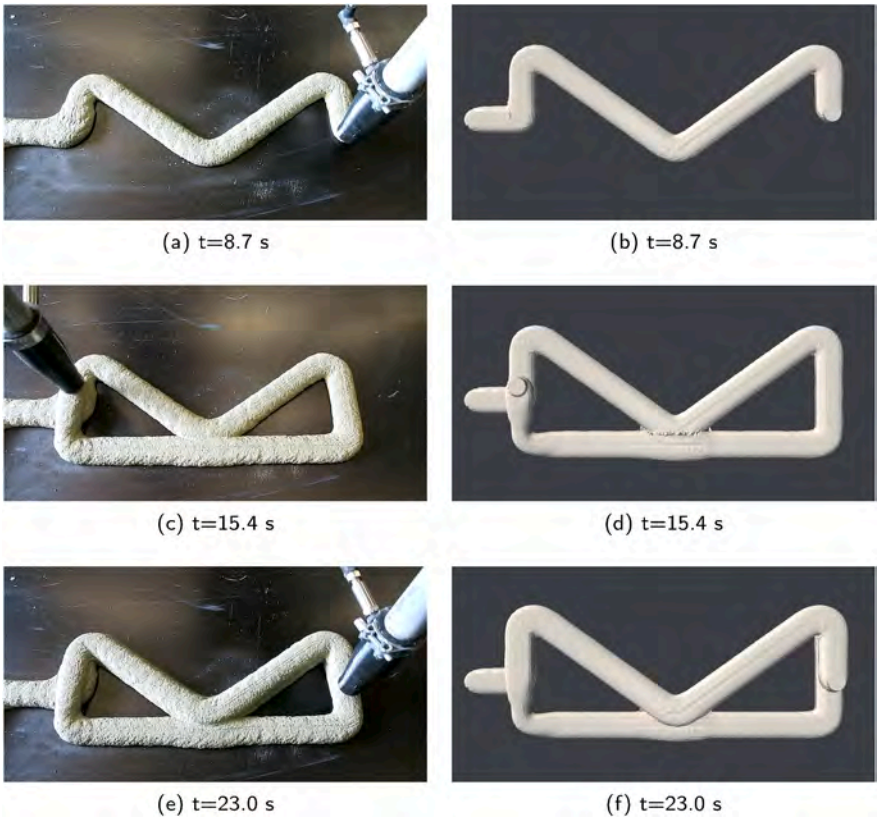

Fig. 15. Real printing process of the first layer (a,c,e); virtual printing process of the first layer (b,d,f).

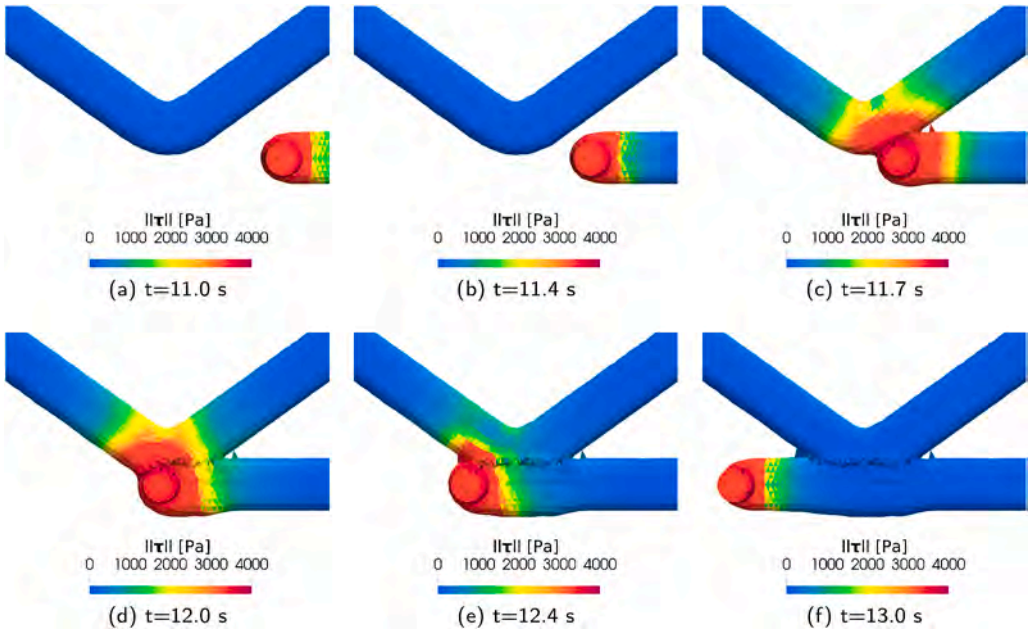

Fig. 16. Virtual printing of the junction between the straight and V-shaped inclined edges, emphasizing the stress-norm distribution. Red regions denote the fluid regime, whereas other colors correspond to the phase-transitioning and solid regimes.

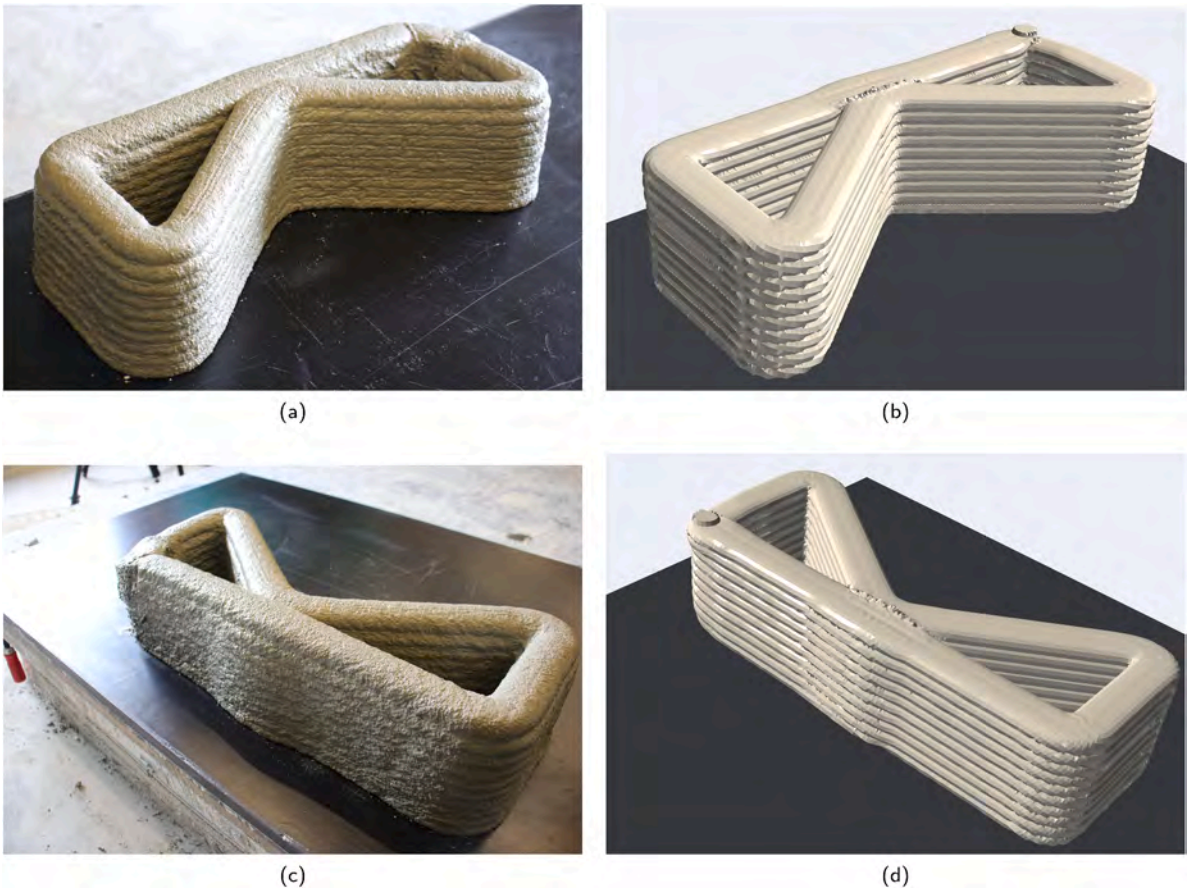

Fig. 17. Comparison of the final printed object obtained experimentally (a, c) with its numerical simulation (b, d).

5. Conclusion

This work introduces a validated framework for simulating 3D printing of cementitious materials, encompassing multiple process scales and material phases. Its two main contributions are a novel fluid-solid constitutive model tailored to 3D-printable cementitious materials and a high-fidelity finite element framework capable of capturing the entire printing process, from extrusion and layer deposition to the global mechanical response.

The constitutive model extends Saramito's elasto-viscoplastic formulation by incorporating time-dependent structuration and pressure-sensitive yielding via a Drucker-Prager criterion, providing a thermodynamically consistent transition from fluid-like to solid-like behaviour. The finite element framework leverages the Particle Finite Element Method (PFEM) to efficiently handle large deformations and evolving free surfaces, enabling seamless simulation of both fluid dynamics during extrusion and solid mechanics phenomena, such as progressive deformation and buckling, within a single computational environment.

Validation against experiments involving vertical and inclined walls demonstrates that the model accurately reproduces layer geometry, uncovering the role of elasticity during layer deposition. The model also predicts structural collapse mechanisms, such as out-of-plane buckling, with good accuracy. Results indicate that frictional effects cannot be neglected, as they play a significant role in stability, particularly for the vertical walls. Incorporating these effects via the Drucker-Prager criterion is therefore essential for reliable buildability predictions. Finally, the simulation of a complex structural component showcases the model's ability to handle intricate geometries and to predict in-plane filament intersections, which are crucial for accurately capturing the true geometry of joint regions.

The main remaining limitation is computational cost, with simulation times ranging from hours to days depending on the size and complexity of the 3D-printed object. This cost arises primarily from the assembly and solution of the linear system, which could be reduced through high-performance computing (HPC) acceleration. The proposed partitioned approach is well suited for parallelization: the constitutive equations are solved explicitly and locally within each finite element [36], while the implicitly solved balance equations can leverage well-established scalable techniques such as parallel Krylov solvers and domain decomposition [65].

Overall, the proposed unified fluid-solid modelling approach enables high-fidelity simulations of extrusion, layer deposition, and buildability, delivering accurate full-order models that capture the underlying physics across relevant process scales. Building on this

foundation, we are exploring machine learning strategies to accelerate computations within the PFEM framework–for instance, by integrating PFEM with graph neural networks [66] - and to develop simplified tools derived from full-order models for predicting specific process-related features [67].

CRediT authorship contribution statement

Giacomo Rizzieri: Writing – original draft, Visualization, Software, Methodology, Conceptualization; **Derk Bos:** Writing – review & editing, Methodology, Investigation; **Rob Wolfs:** Writing – review & editing, Methodology, Investigation; **Liberato Ferrara:** Writing – review & editing, Resources, Methodology; **Massimiliano Cremonesi:** Writing – review & editing, Resources, Methodology, Conceptualization.

Data availability

Data will be made available on request.

Declaration of competing interest

The authors declare that they have no known competing financial interests or personal relationships that could have appeared to influence the work reported in this paper.

Acknowledgements

Funded under project "Material and Process Modelling for Lunar 3D Printing" , CUP D47G25000060006, pursuant to Notice No. 47 of 20/02/2025 (‘Decree for the recruitment of international post-doctoral researchers’), PNRR, Mission 4, Component 2, Investment 1.2, financed by the European Union - NextGeneration EU.

This research was also partially supported by the Italian Ministry of University and Research through the project PRIN2022 DTWIX: development of Digital TWIns for multiphysics simulation of eXtreme events in civil engineering (PRIN DTWIX - 2022AL5MSN).

The 3D printing experiments performed at Eindhoven University of Technology are part of the project “Just Press Print - A multi-scale framework towards first time right 3D Concrete Printing” (with project number 20202) of the Veni talent program, which is financed by the Dutch Research Council (NWO). The authors are grateful to Saint-Gobain Weber Beamix for providing their printable mortar and Siemens Digital Industries for their support in developing the 3DCP system.

The authors thank Alberto Greco, MSc, for his contribution to the experimental 3D-printing campaign during his free-mover secondment at TU/e, carried out in partial fulfilment of the requirements for his Master of Science in Civil Engineering at Politecnico di Milano.

Appendix A. Material properties derivation

This appendix outlines the procedure used to derive the material parameters of the constitutive models, based on experimental measurements and rational estimates.

A.1. Shear modulus

The Young’s modulus $E(t)$ is obtained from the slope of the ascending branch of the stress–strain curves measured in the UUCTs and fitted in Section 4.1 using an exponential function. Lateral strain measurements from the same tests indicate a time-independent Poisson’s ratio of approximately $\nu \approx 0.3$. The Poisson’s ratio is introduced solely for the evaluation of the elastic shear modulus; it does not enter the constitutive formulation directly and does not affect the compressibility of the simulated material. The resulting shear modulus is therefore expressed, with t in minutes, as:

$$G(t) = \frac{E(t)}{2(1+\nu)} = 32\,260 + 29\,410\left(e^{0.03011\,t} - 1\right)\ Pa.$$

A.2. Static yield stress

The compressive yield stress is defined as the exponential fit to the peak stresses of the stress–strain curves and is converted into an equivalent von Mises shear yield stress, with the following expression (t is expressed in minutes):

$$\tau_0(t) = \frac{\sigma_c(t)}{\sqrt{3}} = 4\,158 + 3\,262\left(e^{0.03192\,t} - 1\right)\ Pa.$$

A.3. Mohr–Coulomb parameters

For the frictional formulation, a constant friction angle ϕ is adopted based on the experimental measurements reported in [39]. The cohesion, for the reference strength evolution, is then obtained from the Mohr–Coulomb relation:

$$c(t) = \frac{\sigma_c(t)\left(1-\sin\phi\right)}{2\cos\phi} = 2\,521 + 1\,978\left(e^{0.03192\,t} - 1\right)\ Pa,$$

with t in minutes. For the upper-bound strength evolution, the cohesion is instead given by:

$$c_{\max}(t) = \frac{\sigma_{c,max}(t)\left(1-\sin\phi\right)}{2\cos\phi} = 3\,431 + 4\,652\left(e^{0.02425\,t} - 1\right)\ Pa.$$

A.4. Drucker–Prager parameters

The Drucker–Prager (DP) parameters are derived from the cohesion and friction angle using Eqs. (16)–(17). Since the friction angle is assumed constant, the corresponding DP friction coefficient is time-independent and equal to $\alpha = 0.4457$. The evolution of the DP cohesion parameter $k(t)$ is instead described by:

$$k(t) = 3\,088 + 2\,423\left(e^{0.03192\,t} - 1\right)\ Pa,$$

with t in minutes. For the upper-bound strength evolution, the following expression is adopted:

$$k_{\max}(t) = 4\,202 + 5\,698\left(e^{0.02425\,t} - 1\right)\ Pa.$$

A.5. Viscosity

As shown in [18], viscosity has a negligible influence on the filament cross-section when printing high-yield-stress materials under standard conditions. This was confirmed for the present study printing set-up through preliminary simulations of single-layer extrusion using three representative viscosity values, $\eta = 5$, 10 and 20 $Pa \cdot s$. The resulting filament geometries (Fig. A.18-a) were essentially identical, motivating the use of $\eta = 10\ Pa \cdot s$.

In principle, the microstructural viscosity could be determined from a dynamic sweep test on a rheometer. However, because fresh concrete is a water-based suspension, the solvent viscosity in the fluid regime is expected to lie between that of water and the total measured viscosity. With the total viscosity set to 10 $Pa \cdot s$, the microstructural contribution can therefore be estimated by difference.

To assess the influence of viscosity partitioning, a sensitivity analysis was performed over the range 0.001–10 $Pa \cdot s$. The results (Fig. A.18-b) confirm that, for the shear modulus value considered here, the specific division between solvent and microstructural viscosity has a negligible effect on the model predictions.

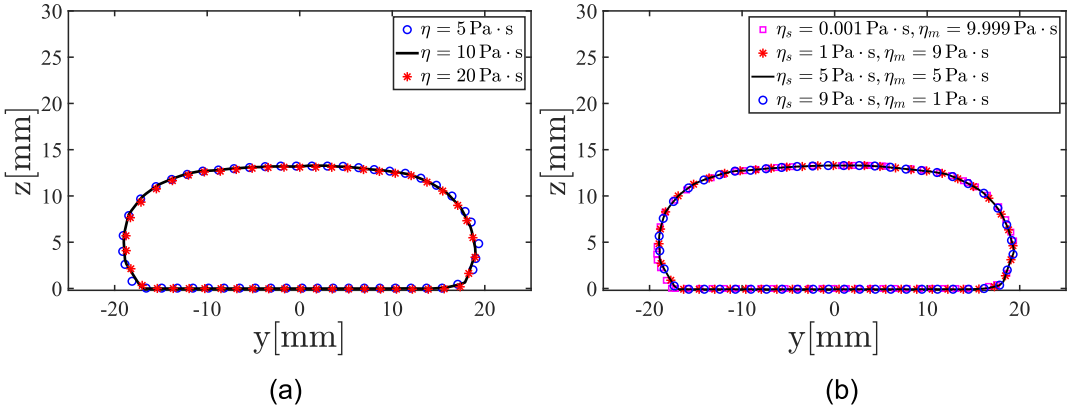

Fig. A.18. Effect of the total viscosity (a) and of the partitioning between solvent and microstructural viscosity (b) on the shape of the first layer.

References

[1] T. Wangler, E. Lloret, L. Reiter, N. Hack, F. Gramazio, M. Kohler, M. Bernhard, B. Dillenburger, J. Buchli, N. Roussel, R. Flatt, Digital concrete: opportunities and challenges, RILEM Tech. Lett. 1 (2016) 67–75. https://doi.org/10.21809/rilemtechlett.2016.16

[2] R. Wolfs, D. Bos, J.-F. Caron, M. Gerke, R. Mesnil, R. Buswell, N. Ducoulombier, N. Hack, E. Keita, P. Kinnell, K. Mawas, V. Mechtcherine, L. Miranda, D. Sokolov, J. Versteege, N. Roussel, On-line and in-line quality assessment across all scale levels of 3D concrete printing, Cem. Concr. Res. 185 (2024) 107646. https://doi.org/10.1016/j.cemconres.2024.107646

[3] A. Perrot, A. Pierre, V.N. Nerella, R.J.M. Wolfs, E. Keita, S.A.O. Nair, N. Neithalath, N. Roussel, V. Mechtcherine, From analytical methods to numerical simulations: a process engineering toolbox for 3D concrete printing, Cem. Concr. Compos. 122 (2021) 104164. https://doi.org/10.1016/j.cemconcomp.2021.104164

[4] R.J.M. Wolfs, F.P. Bos, T.A.M. Salet, Early age mechanical behaviour of 3D printed concrete: numerical modelling and experimental testing, Cem. Concr. Res. 106 (2018) 103–116. https://doi.org/10.1016/j.cemconres.2018.02.001

[5] R.J.M. Wolfs, A.S.J. Suiker, Structural failure during extrusion-based 3D printing processes, Int. J. Adv. Manuf. Technol. 104 (1) (2019) 565–584. https://doi.org/10.1007/s00170-019-03844-6

[6] T. Ooms, G. Vantyghem, R. Van Coile, W. De Corte, A parametric modelling strategy for the numerical simulation of 3D concrete printing with complex geometries, Addit. Manuf. 38 (2021). https://doi.org/10.1016/j.addma.2020.101743

[7] V. Nguyen-Van, B. Panda, G. Zhang, H. Nguyen-Xuan, P. Tran, Digital design computing and modelling for 3-D concrete printing, Autom. Constr. 123 (2021) 103529. https://doi.org/10.1016/j.autcon.2020.103529

[8] J. Rymeš, J. Cervenka, L. Jendele, Material modelling and simulation of 3D concrete printing process, in: Proceedings of the 11th International Conference on Fracture Mechanics of Concrete and Concrete Structures, IA-FraMCoS, 2023. https://doi.org/10.21012/FC11.092346

[9] Q. Chen, G.B. Barbat, M. Cervera, Finite element buildability analysis of 3D printed concrete including failure by elastic buckling and plastic flow, Eng. Struct. 340 (2025) 120675. https://doi.org/10.1016/j.engstruct.2025.120675

[10] M. Pierre, S. Ghabezloo, P. Dangla, R. Mesnil, M. Vandamme, J.-F. Caron, Multiphysics modelling of 3D concrete printing: from material model to process simulation and optimisation, Addit. Manuf. 109 (2025) 104847. https://doi.org/10.1016/j.addma.2025.104847

[11] X. Liu, B. Sun, The influence of interface on the structural stability in 3D concrete printing processes, Addit. Manuf. 48 (2021) 102456. https://doi.org/10.1016/j.addma.2021.102456

[12] J. Reinold, K. Daadouch, G. Meschke, Numerical simulation of three dimensional concrete printing based on a unified fluid and solid mechanics formulation, Front. Struct. Civ. Eng. 18 (4) (2024) 491–515. https://doi.org/10.1007/s11709-024-1082-2

[13] R. Comminal, W.R. Leal da Silva, T.J. Andersen, H. Stang, J. Spangenberg, Modelling of 3D concrete printing based on computational fluid dynamics, Cem. Concr. Res. 138 (2020). https://doi.org/10.1016/j.cemconres.2020.106256

[14] M.T. Mollah, R. Comminal, M.P. Serdeczny, D.B. Pedersen, J. Spangenberg, Stability and deformations of deposited layers in material extrusion additive manufacturing, Addit. Manuf. 46 (2021) 102193. https://doi.org/10.1016/j.addma.2021.102193

[15] R.J.M. Wolfs, T.A.M. Salet, N. Roussel, Filament geometry control in extrusion-based additive manufacturing of concrete: the good, the bad and the ugly, Cem. Concr. Res. 150 (2021). https://doi.org/10.1016/j.cemconres.2021.106615

[16] J. Reinold, V.N. Nerella, V. Mechtcherine, G. Meschke, Extrusion process simulation and layer shape prediction during 3D-concrete-printing using the particle finite element method, Autom. Constr. 136 (2022). https://doi.org/10.1016/j.autcon.2022.104173

[17] G. Rizzieri, L. Ferrara, M. Cremonesi, Numerical simulation of the extrusion and layer deposition processes in 3D concrete printing with the Particle Finite Element Method, Comput. Mech. 73 (2) (2024) 277–295. https://doi.org/10.1007/s00466-023-02367-y

[18] G. Rizzieri, S. Meni, M. Cremonesi, L. Ferrara, A Particle Finite Element Method for investigating the influence of material and process parameters in 3D concrete printing, Comp. Struct. 316 (2025) 107883. https://doi.org/10.1016/j.compstruc.2025.107883

[19] G. Rizzieri, M. Cremonesi, L. Ferrara, A 2D numerical model of 3D concrete printing including thixotropy, Mater. Today (2023). https://doi.org/10.1016/j.matpr.2023.08.082

[20] G. Rizzieri, M. Cremonesi, L. Ferrara, Challenging the limits of fluid FEM modelling in 3D concrete printing, in: D. Lowke, N. Freund, D. Böhler, F. Herding (Eds.), Fourth RILEM International Conference on Concrete and Digital Fabrication. DC 2024., Springer Nature Switzerland, Cham, 2024, pp. 482–489. https://doi.org/10.1007/978-3-031-70031-6_56

[21] E. Ramyar, G. Cusatis, Discrete fresh concrete model for simulation of ordinary, self-consolidating, and printable concrete flow, J. Eng. Mech. 148 (2) (2022). https://doi.org/10.1061/(asce)em.1943-7889.0002059

[22] K. Krenzer, U. Palzer, S. Müller, V. Mechtcherine, Simulation of 3D concrete printing using Discrete Element Method, in: R. Buswell, A. Blanco, S. Cavalaro, P. Kinnell (Eds.), Third RILEM International Conference on Concrete and Digital Fabrication, Springer International Publishing, Cham, 2022, pp. 161–166. https://doi.org/10.1007/978-3-031-06116-5_24

[23] J. Zhu, X. Ren, M. Cervera, Buildability modeling of 3D-printed concrete including printing deviation: a stochastic analysis, Constr. Build. Mater. 403 (2023) 133076. https://doi.org/10.1016/j.conbuildmat.2023.133076

[24] Z. Chang, Y. Xu, Y. Chen, Y. Gan, E. Schlangen, B. Šavija, A discrete lattice model for assessment of buildability performance of 3D-printed concrete, Comput.-Aided Civ. Infrastruct. Eng. 36 (5) (2021) 638–655. https://doi.org/10.1111/mice.12700

[25] J. Donea, A. Huerta, J.-P. Ponthot, A. Rodríguez-Ferran, Arbitrary Lagrangian–Eulerian methods, in: E. Stein, R. de Borst, T.J.R. Hughes (Eds.), Encyclopedia of Computational Mechanics, John Wiley & Sons, Ltd, 2017, pp. 1–23. https://doi.org/10.1002/9781119176817.ecm2009

[26] F. Mahaut, X. Chateau, P. Coussot, G. Ovarlez, Yield stress and elastic modulus of suspensions of noncolloidal particles in yield stress fluids, J. Rheol. 52 (1) (2008) 287–313. https://doi.org/10.1122/1.2798234

[27] N. Roussel, G. Ovarlez, S. Garrault, C. Brumaud, The origins of thixotropy of fresh cement pastes, Cem. Concr. Res. 42 (1) (2012) 148–157. https://doi.org/10.1016/j.cemconres.2011.09.004

[28] P. Saramito, A new constitutive equation for elastoviscoplastic fluid flows, J. Non-Newtonian Fluid Mech. 145 (1) (2007) 1–14. https://doi.org/10.1016/j.jnnfm.2007.04.004

[29] P. Saramito, A new elastoviscoplastic model based on the Herschel–Bulkley viscoplastic model, J. Non-Newtonian Fluid Mech. 158 (1–3) (2009) 154–161. https://doi.org/10.1016/j.jnnfm.2008.12.001

[30] D. Fraggedakis, Y. Dimakopoulos, J. Tsamopoulos, Yielding the yield stress analysis: a thorough comparison of recently proposed elasto-visco-plastic (EVP) fluid models, J. Non-Newtonian Fluid Mech. 236 (2016) 104–122. https://doi.org/10.1016/j.jnnfm.2016.09.001

[31] E. Mitsoulis, Numerical simulations of complex yield-stress fluid flows, Rheol. Acta (2017) 231–258. https://doi.org/10.1007/s00397-016-0981-0

[32] N. Roussel, A thixotropy model for fresh fluid concretes: theory, validation and applications, Cem. Concr. Res. 36 (10) (2006) 1797–1806. https://doi.org/10.1016/j.cemconres.2006.05.025

[33] A. Perrot, D. Rangeard, A. Pierre, Structural built-up of cement-based materials used for 3D-printing extrusion techniques, Mater. Struct. 49 (4) (2016) 1213–1220. https://doi.org/10.1617/s11527-015-0571-0

[34] J.G. Oldroyd, On the formulation of rheological equations of state, Proc. R. Soc. Lond. 200 (1950) 523–541. https://doi.org/10.1098/rspa.1950.0035

[35] E.A. De Souza Neto, D. Perić, D.R.J. Owen, Computational Methods for Plasticity: Theory and Applications, Wiley, 1 edition, 2008. https://doi.org/10.1002/9780470694626

[36] G. Rizzieri, L. Ferrara, M. Cremonesi, A partitioned Lagrangian finite element approach for the simulation of viscoelastic and elasto-viscoplastic free-surface flows, Comput. Methods Appl. Mech. Eng. 443 (2025) 118071. https://doi.org/10.1016/j.cma.2025.118071

[37] T.C. Papanastasiou, Flows of materials with yield, J. Rheol. 31 (5) (1987) 385–404. https://doi.org/10.1122/1.549926

[38] R. Nicolas, B. Richard, D. Nicolas, I. Irina, K.J. Temitope, L. Dirk, M. Viktor, M. Romain, P. Arnaud, P. Ursula, R. Lex, S. Dietmar, W. Timothy, W. Rob, Z. Wenqiang, Assessing the fresh properties of printable cement-based materials: high potential tests for quality control, Cem. Concr. Res. 158 (2022) 106836. https://doi.org/10.1016/j.cemconres.2022.106836

[39] A.H. Deetman, A.S.J. Suiker, Characterization of early-age elastic–plastic properties of 3D printed materials using indentation testing, Int. J. Mech. Sci. 310 (2026) 111141. https://doi.org/10.1016/j.ijmecsci.2025.111141

[40] J. McConnell, W. Ortiz, J.C. Sutherland, P. Newell, A.M. Grillet, A.M. McMaster, R.B. Bhakta, R.R. Rao, Computational modeling and experiments of an elastoviscoplastic fluid in a thin mold-filling geometry, J. Non-Newtonian Fluid Mech. 307 (2022) 104851. https://doi.org/10.1016/j.jnnfm.2022.104851

[41] L. Esposito, L. Casagrande, C. Menna, D. Asprone, F. Auricchio, Early-asge creep behaviour of 3D printable mortars: experimental characterisation and analytical modelling, Mater. Struct. 54 (6) (2021) 207. https://doi.org/10.1617/s11527-021-01800-z

[42] Z. Chang, M. Liang, Y. Xu, Z. Wan, E. Schlangen, B. Šavija, Early-age creep of 3D printable mortar: experiments and analytical modelling, Cem. Concr. Compos. 138 (2023) 104973. https://doi.org/10.1016/j.cemconcomp.2023.104973

[43] P.R. De Souza Mendes, modelling the thixotropic behavior of structured fluids, J. Non-Newtonian Fluid Mech. 164 (1–3) (2009) 66–75. https://doi.org/10.1016/j.jnnfm.2009.08.005

[44] J.T. Kolawole, R. Combrinck, W.P. Boshoff, Rheo-viscoelastic behaviour of fresh cement-based materials: cement paste, mortar and concrete, Constr. Build. Mater. 248 (2020) 118667. https://doi.org/10.1016/j.conbuildmat.2020.118667
[45] R. Guénette, M. Fortin, A new mixed finite element method for computing viscoelastic flows, J. Non-Newtonian Fluid Mech. 60 (1) (1995) 27–52. https://doi.org/10.1016/0377-0257(95)01372-3
[46] M. Cremonesi, A. Franci, S. Idelsohn, E. Oñate, A state of the art review of the Particle Finite Element Method (PFEM), Arch. Comput. Methods Eng. 27 (5) (2020) 1709–1735. https://doi.org/10.1007/s11831-020-09468-4
[47] M. Fortin, F. Brezzi, Mixed and Hybrid Finite Element Methods, 51, New York: Springer-Verlag, 1991.
[48] T.J.R. Hughes, L.P. Franca, M. Balestra, A new finite element formulation for computational fluid dynamics: v. circumventing the Babuška-Brezzi condition: a stable Petrov-Galerkin formulation of the stokes problem accommodating equal-order interpolations, Comput. Methods Appl. Mech. Eng. 59 (1) (1986) 85–99. https://doi.org/10.1016/0045-7825(86)90025-3
[49] T.E. Tezduyar, S. Mittal, S.E. Ray, R. Shih, Incompressible flow computations with stabilized bilinear and linear equal-order-interpolation velocity-pressure elements, Comput. Methods Appl. Mech. Eng. 95 (2) (1992) 221–242. https://doi.org/10.1016/0045-7825(92)90141-6
[50] E. Oñate, S.R. Idelsohn, F. Del Pin, R. Aubry, The particle finite element method. an overview, Int. J. Comput. Methods 1 (2) (2004) 267–307. https://doi.org/10.1142/S0219876204000204
[51] M.L. Cerquaglia, D. Thomas, R. Boman, V. Terrapon, J.P. Ponthot, A fully partitioned Lagrangian framework for FSI problems characterized by free surfaces, large solid deformations and displacements, and strong added-mass effects, Comput. Methods Appl. Mech. Eng. 348 (2019) 409–442. https://doi.org/10.1016/j.cma.2019.01.021
[52] D.H.F.R. Moreira, G. Avancini, R.A.K. Sanches, A monolithic PFEM-FEM approach for fluid–structure interaction with structural contact: applications in engineering and biomechanics, Comput. Part Mech. (2025). https://doi.org/10.1007/s40571-025-01081-1
[53] G. Rizzieri, L. Ferrara, M. Cremonesi, Simulation of viscoelastic free-surface flows with the Particle Finite Element Method, Comput. Part Mech. 11 (5) (2024) 2043–2067. https://doi.org/10.1007/s40571-024-00730-1
[54] S. Larsson, J.M. Rodríguez Prieto, G. Gustafsson, H.Å. Häggblad, P. Jonsén, The Particle Finite Element Method for transient granular material flow: modelling and validation, Comput. Part Mech. 8 (1) (2021) 135–155. https://doi.org/10.1007/s40571-020-00317-6
[55] T. Leyssens, M.W. Henry, J. Lambrechts, V. Legat, J.-F. Remacle, A Coupled Pfem-Dem Model for Fluid-Granular Flows with Free-Surface Dynamics Applied to Landslides, 2025. https://doi.org/10.2139/ssrn.5082698
[56] E. Oñate, A. Franci, J.M. Carbonell, A Particle Finite Element Method for analysis of industrial forming processes, Comput. Mech. 54 (1) (2014) 85–107. https://doi.org/10.1007/s00466-014-1016-2
[57] O. Sandin, P. Larour, J.M. Rodríguez, S. Parareda, S. Hammarberg, J. Kajberg, D. Casellas, Numerical modelling of shear cutting in complex phase high strength steel sheets: a comprehensive study using the Particle Finite Element Method, Finite Elem. Anal. Des. 246 (2025) 104331. https://doi.org/10.1016/j.finel.2025.104331
[58] M. Schewe, I. Noll, T. Bartel, A. Menzel, Towards the simulation of metal deposition with the Particle Finite Element Method and a phase transformation model, Comput. Methods Appl. Mech. Eng. 437 (2025) 117730. https://doi.org/10.1016/j.cma.2025.117730
[59] S. Février, E. Fernández, M. Lacroix, R. Boman, J.-P. Ponthot, Simulation of melt pool dynamics including vaporization using the Particle Finite Element Method, Comput. Mech. 75 (2025) 1787–1815. https://doi.org/10.1007/s00466-024-02571-4
[60] H. Si, Tetgen, a delaunay-based quality tetrahedral mesh generator, ACM Trans. Math. Software 41 (2) (2015). https://doi.org/10.1145/2629697
[61] H. Edelsbrunner, E.P. Mücke, Three-dimensional alpha shapes, ACM Trans. Graph. 13 (1) (1994) 43–72. https://doi.org/10.1145/174462.156635
[62] J. Oliver, J.C. Cante, R. Weyler, C. González, J. Hernandez, Particle Finite Element Methods in solid mechanics problems, in: E. Oñate, R. Owen (Eds.), Computational Plasticity, Springer Netherlands, Dordrecht, 2007, pp. 87–103. https://doi.org/10.1007/978-1-4020-6577-4_6
[63] A. Franci, M. Cremonesi, On the effect of standard PFEM remeshing on volume conservation in free-surface fluid flow problems, Comput. Part Mech. 4 (3) (2017) 331–343. https://doi.org/10.1007/s40571-016-0124-5
[64] J. Versteege, R.J.M. Wolfs, T.A.M. Salet, Data-driven additive manufacturing with concrete: enhancing in-line sensory data with domain knowledge, part i: geometry, Autom. Constr. 172 (2025) 106020. https://doi.org/10.1016/j.autcon.2025.106020
[65] H.S. Tang, R.D. Haynes, G. Houzeaux, A review of domain decomposition methods for simulation of fluid flows: concepts, algorithms, and applications, Arch. Comput. Methods Eng. 28 (3) (2021) 841–873. https://doi.org/10.1007/s11831-019-09394-0
[66] F. Lanteri, M. Cremonesi, A mesh-based graph neural network approach for surrogate modeling of Lagrangian free surface fluid flows, (Taipei) & Fluids. 301 (2025) 106773. https://doi.org/10.1016/j.compfluid.2025.106773
[67] G. Rizzieri, F. Lanteri, L. Ferrara, M. Cremonesi, ShapeGen3DCP: a deep learning framework for layer shape prediction in 3D concrete printing, Comp. Struct. 323 (2026) 108142. https://doi.org/10.1016/j.compstruc.2026.108142